Defense Threat Reduction Agency
8725 John J. Kingman Road, MS 6201
Fort Belvoir, VA 22060-6201

DTRA-TR-00-3

TECHNICAL REPORT

A 2D Electron Density and Plasma Current Density Diagnostic for Opening Switches

Approved for public release; distribution is unlimited.

February 2006

DSWA01-96-C-0175

John J. Moschella
Conrad C. Klepper

Prepared by:
HY-Tech Research Corporation
104 Centre Court
Radford, Virginia 24141

DESTRUCTION NOTICE

FOR CLASSIFIED documents, follow the procedures in DoD 5550.22-M, National Industrial Security Program Operating Manual, Chapter 5, Section 7 (NISPOM) or DoD 5200.1-R, Information Security Program Regulation, Chapter 1X.

FOR UNCLASSIFIED limited documents, destroyed by any method that will prevent disclosure of contents or reconstruction of the document.

Retention of this document by DoD contractors is authorized in accordance with DoD 5220.22-M, Industrial Security Manual.

PLEASE NOTIFY THE DEFENSE THREAT REDUCTION AGENCY, ATTN: BDLMI, 8725 JOHN J. KINGMAN ROAD, MS-6201, FT BELVOIR, VA 22060-6201, IF YOUR ADDRESS IS INCORRECT, IF YOU WISH IT DELETED FROM THE DISTRIBUTION LIST, OR IF THE ADDRESSEE IS NO LONGER EMPLOYED BY YOUR ORGANIZATION.

DISTRIBUTION LIST UPDATE

This mailer is provided to enable DTRA to maintain current distribution lists for reports. (We would appreciate you providing the requested information.)

- ❑ Add the individual listed to your distribution list.
- ❑ Delete the cited organization/individual.
- ❑ Change of address.

Note:
Please return the mailing label from the document so that any additions, changes, corrections or deletions can be made easily. For distribution cancellation or more information call DTRA/BDLMI (703) 767-4725.

NAME: _____

ORGANIZATION: _____

OLD ADDRESS	NEW ADDRESS
_____	_____
_____	_____
_____	_____

TELEPHONE NUMBER: ( ) _____

DTRA PUBLICATION NUMBER/TITLE	CHANGES/DELETIONS/ADDITONS, etc. *(Attach Sheet if more Space is Required)*
_____	_____
_____	_____
_____	_____

DTRA or other GOVERNMENT CONTRACT NUMBER: _____

CERTIFICATION of NEED-TO-KNOW BY GOVERNMENT SPONSOR (if other than DTRA):

SPONSORING ORGANIZATION: _____

CONTRACTING OFFICER or REPRESENTATIVE: _____

SIGNATURE: _____

REPORT DOCUMENTATION PAGE

Form Approved
OMB No. 0704-0188

1. AGENCY USE ONLY *(Leave blank)*	2. REPORT DATE	3. REPORT TYPE AND DATES COVERED
		Final 960910-991220

4. TITLE AND SUBTITLE

A 2D Electron Density and Plasma Current Density Diagnostic for Opening Switches

5. FUNDING NUMBERS

C- DSWA01-96-C-0175
PE - 1340
PR- OH
TA- OO
WU- DH63332

6. AUTHOR(S)

John J. Moschella and Conrad C. Klepper

7. PERFORMING ORGANIZATION NAME(S) AND ADDRESS(ES)

HY-Tech Research Corporation
104 Centre Court
Radford, VA 24141

8. PERFORMING ORGANIZATION REPORT NUMBER

9. SPONSORING / MONITORING AGENCY NAME(S) AND ADDRESS(ES)

Defense Threat Reduction Agency
8725 John J. Kingman Rd., STOP 6201
Fort Belvoir, VA 22060-6201
NT/ Davis

10. SPONSORING / MONITORING AGENCY REPORT NUMBER

DTRA-TR-00-3

11. SUPPLEMENTARY NOTES

This work was sponsored by the Defense Threat Reduction Agency under RDT&E RMSS Code B 1340 D 1D20 OH OO 63332 25904D

12a. DISTRIBUTION / AVAILABILITY STATEMENT

Approved for public release; distribution is unlimited.

12b. DISTRIBUTION CODE

13. ABSTRACT *(Maximum 200 words)*

A program to develop diagnostics for plasma opening switches has been completed. HY-Tech has investigated 2D interferometry using a short pulsed laser for determining the electron density distribution and multi-chord spectroscopic observations for determining the plasma current density. The electron density diagnostic used a short pulsed (10 ns) Nd:YAG laser to form interferograms using a Mach-Zehnder arrangement. These interference patterns were captured using a scientific grade CCD camera. HY-Tech developed computer algorithms to analyze interferometric fringe patterns using two dimensional fast Fourier transforms that could achieve a sensitivity to electrons of better than 6 X 10^{15} cm^{-2} (10^{o} at 1064 nm). The plasma current diagnostic is based on the spectroscopic observation of seeded ions in the POS plasma that are used to map out the magnetic field distribution. The magnetic field can be calculated by observation of Zeeman splitting or the acceleration of seeded ions, with each method best suited for opening switches operating in different regimes. The spectroscopic observation system included a McPherson 0.67 m imaging monochromatic and a Princeton Instruments ICCD camera. Numerous calculations and measurements were performed to optimize the injected material for the type of plasma. Details are included in this report.

14. SUBJECT TERMS			15. NUMBER OF PAGES
	POS	Interferometry	57
	FFT	Spectroscopy	16. PRICE CODE

17. SECURITY CLASSIFICATION OF REPORT	18. SECURITY CLASSIFICATION OF THIS PAGE	19. SECURITY CLASSIFICATION OF ABSTRACT	20. LIMITATION OF ABSTRACT
Unclassified	Unclassified	Unclassified	SAR

CONVERSION TABLE

Conversion Factors for U.S. Customary to metric (SI) units of measurement.

MULTIPLY →	BY →	TO GET
TO GET ←	BY ←	DIVIDE

angstrom	1.000 000 x E -10	meters (m)
atmosphere (normal)	1.013 25 x E +2	kilo pascal (kPa)
bar	1.000 000 x E +2	kilo pascal (kPa)
barn	1.000 000 x E -28	meter^2 (m^2)
British thermal unit (thermochemical)	1.054 350 x E +3	joule (J)
calorie (thermochemical)	4.184 000	joule (J)
cal (thermochemical/cm^2)	4.184 000 x E -2	mega joule/m^2 (MJ/m^2)
curie	3.700 000 x E +1	*giga bacquerel (GBq)
degree (angle)	1.745 329 x E -2	radian (rad)
degree Fahrenheit	$t_k = (t°f + 459.67)/1.8$	degree kelvin (K)
electron volt	1.602 19 x E -19	joule (J)
erg	1.000 000 x E -7	joule (J)
erg/second	1.000 000 x E -7	watt (W)
foot	3.048 000 x E -1	meter (m)
foot-pound-force	1.355 818	joule (J)
gallon (U.S. liquid)	3.785 412 x E -3	meter^3 (m^3)
inch	2.540 000 x E -2	meter (m)
jerk	1.000 000 x E +9	joule (J)
joule/kilogram (J/kg) radiation dose absorbed	1.000 000	Gray (Gy)
kilotons	4.183	terajoules
kip (1000 lbf)	4.448 222 x E +3	newton (N)
kip/inch^2 (ksi)	6.894 757 x E +3	kilo pascal (kPa)
ktap	1.000 000 x E +2	newton-second/m^2 (N-s/m^2)
micron	1.000 000 x E -6	meter (m)
mil	2.540 000 x E -5	meter (m)
mile (international)	1.609 344 x E +3	meter (m)
ounce	2.834 952 x E -2	kilogram (kg)
pound-force (lbs avoirdupois)	4.448 222	newton (N)
pound-force inch	1.129 848 x E -1	newton-meter (N-m)
pound-force/inch	1.751 268 x E +2	newton/meter (N/m)
pound-force/foot^2	4.788 026 x E -2	kilo pascal (kPa)
pound-force/inch^2 (psi)	6.894 757	kilo pascal (kPa)
pound-mass (lbm avoirdupois)	4.535 924 x E -1	kilogram (kg)
pound-mass-foot^2 (moment of inertia)	4.214 011 x E -2	kilogram-meter^2 (kg-m^2)
pound-mass/foot^3	1.601 846 x E +1	kilogram-meter^3 (kg/m^3)
rad (radiation dose absorbed)	1.000 000 x E -2	**Gray (Gy)
roentgen	2.579 760 x E -4	coulomb/kilogram (C/kg)
shake	1.000 000 x E -8	second (s)
slug	1.459 390 x E +1	kilogram (kg)
torr (mm Hg, 0^0 C)	1.333 22 x E -1	kilo pascal (kPa)

*The bacquerel (Bq) is the SI unit of radioactivity; 1 Bq = 1 event/s.
**The Gray (GY) is the SI unit of absorbed radiation.

Table of Contents

Figures

Section 1
Executive Summary

Diagnostic systems for measuring electron density and current density have been designed and tested for use in plasma opening switches (POS). The electron density diagnostic is based on interferometric techniques while the current density diagnostic is based on determining the magnetic field and then deducing the current density. Both of these systems emphasize measurements in two dimensions with methods that are either innovative, or modified to suit the conditions in a POS. These conditions require a sensitivity to electrons of at least 10^{16} cm^{-2} and a sensitivity to the magnetic field of at least 0.5 T.

The electron density diagnostic has been designed, built, and tested. These tests included measurements on a planar POS at HY-Tech,[1] and the downstream region of the ACE-4 POS at Maxwell Technologies.[2] We have shown a sensitivity to electrons of better than 6×10^{15} cm^{-2} (10° at 1064 nm) with a spatial resolution of better than 100 μm over a 25 cm^2 region. To accomplish this, we constructed a standard Mach-Zehnder interferometer where the interference pattern was captured on a high-resolution CCD camera. With the data stored digitally, we were able to analyze the interferograms using fast Fourier transforms (FFT) to improve the phase resolution to the levels quoted above.[3] Software to analyze these interferograms was developed on a PC and used during the tests.

One limitation of this diagnostic is that the viewing area is reduced significantly when the reference and scene beams are combined. Initially the laser beam is approximately 9.5 cm in diameter (75 cm^2), however due to the large recombining angle of the scene and reference beams required for the FFT analysis, this area is reduced to 25 cm^2. This can be overcome by using larger optics, in particular the recombining beamsplitter. The present system tested used nominal 4" optics for all beamsplitters and mirrors.

The current density, or magnetic field, diagnostic has not been as successful from the standpoint of producing actual field tests and measurements on a POS. There were a number of reasons for this. Among the most important was that this measurement required a great deal of technical innovation (plasma seeding and multi-chord observation) and coordinated modeling efforts. While we did not actually make a field measurement, we will

offer a recipe for such a measurement based on seeding techniques developed during the program, and observations of the POS plasma that can be used to choose the seed material. During the program we explored various techniques to seed the plasma while measuring characteristics of the ablated plume spectroscopically. We also conducted a spectroscopic investigation on the planar switch at HY-Tech by observing seeded ions and native carbon ion emission. These experimental results, along with modeling results, allowed us to determine the effective electron temperature of the plasma and narrow down the possible seed materials that were best suited for a magnetic field measurement. We also fabricated the components to view the plasma along several chords simultaneously.

Section 2
Introduction

2.1 Electron Density Diagnostics for the POS.

In past experiments, electron density measurements on plasma opening switches have been obtained using time resolved heterodyne interferometry almost exclusively with HeNe lasers.[4, 5] This diagnostic has very good sensitivity to electrons ($\sim 10^{15}$ cm^{-2}), is relatively inexpensive to set-up, and easy to operate. In its most basic form, heterodyne interferometry provides density information in one location as a function of time. It has also provided valuable information on the operation of the POS throughout the years. However, the spatial resolution is limited. At 1 mm it is not suitable for direct observation of surface/plasma phenomena in the switch and downstream MITL. These have become important considerations with regards to improving switches.[6] One point of concern has been the purity of electrode surfaces and the deleterious effects of plasma that may be generated from these impurities. Surface plasma formation downstream of the POS may indicate current flow, which in itself is an important observation.

These types of phenomena require diagnostics with a high degree of spatial resolution. Such spatial resolution is provided by 2D interferometry, however, the sensitivity of such an interferometer has always been an issue. The FFT analysis method that we have developed improves sensitivity by a factor of 5 when compared to traditional graphical analysis techniques which makes it competitive with heterodyne interferometry, although the latter is still a factor of 4 better. The 2D technique is not time resolved, it provides density information over a large area, but only at one instant in time. Therefore the two techniques are complimentary; where one (heterodyne) provides time resolved information at a single point in space, the other (2D interferometry) provides spatially resolved information at one point in time.

The basic 2D Mach-Zehnder interferometer is shown in Figure 1. The heart of the apparatus is a pulsed Nd:YAG laser (Spectra-Physics Model GCR-170-10) with an injection seeder. The output wavelength of the laser is 1064 nm and the system contains a frequency doubling crystal that can be used to produce a 532 nm beam, the former is more

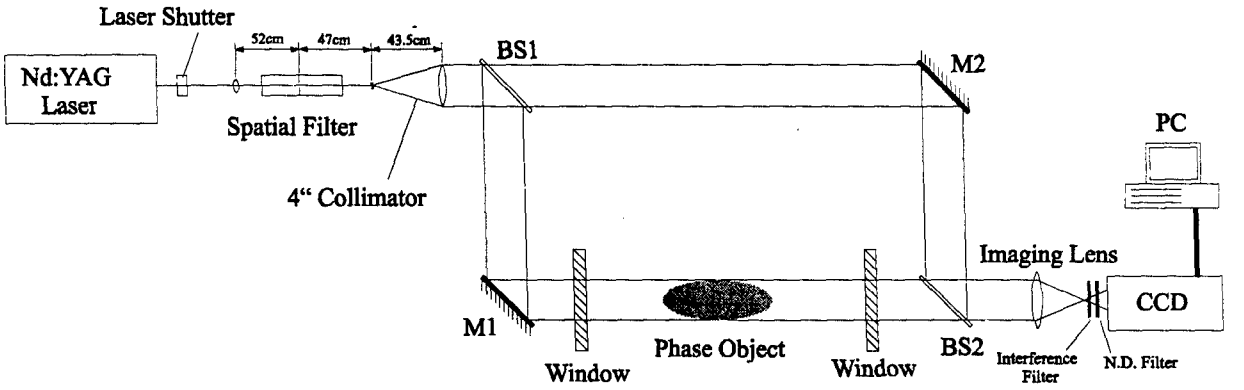

Figure 1. A schematic of the two dimensional Mach-Zehnder interferometer setup.

sensitive to electrons. The injection seeder ensures operation in a single longitudinal mode that has the effect of increasing the spatial coherence length from 1 cm to 1 m. The optics function to collimate a large diameter beam (nominal 4 inch) and split the beam into a scene and reference arm. These beams are recombined at an angle to form an interference pattern that is recorded by a high resolution CCD camera (Princeton Instruments PentaMAX 1317K1). The data is then analyzed by a computer program that includes FFT routines and produces phase data within minutes of the event.

2.2 Current Density Diagnostics for the POS.

Plasma current diagnostics rely on the measurement of magnetic field to determine information on the current flow in a plasma. If a sufficiently detailed measurement of the magnetic field distribution is made, then Ampere's law can be used to calculate the current density. Even if this is not the case, information on the current flow can still be obtained. In switch plasmas, magnetic pick-up loops (B-dot loops) have been used to deduce the magnetic field by inserting them in the plasma.[7, 8] Alternatives to this approach have been sought because the B-dot loops perturb the plasma. Spectroscopic techniques for measuring the magnetic field have been developed by Y. Maron and co-workers at the Weizmann Institute of Science and have been applied to relatively low power switches.[9, 10, 11, 12, 13] These techniques rely on observing light emitted by the seeded material as a result of electron impact excitation in the POS plasma. The magnetic field can be deduced via one of two methods: (1) the acceleration of the seeded ions or (2) the Zeeman splitting of energy levels. The suitability of each method depends on the plasma

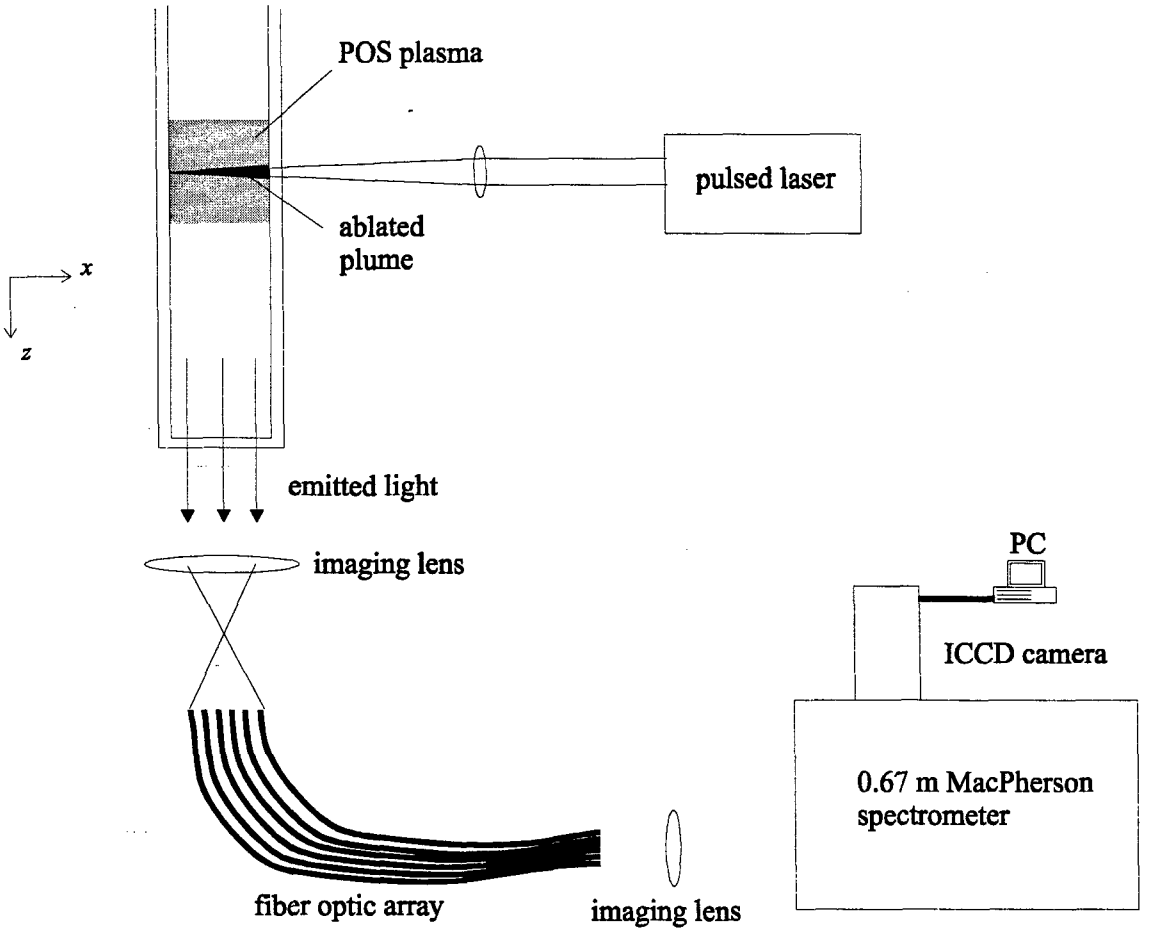

Figure 2. A schematic of the set up for the current diagnostic on a cylindrical POS.

characteristics such as the electron density and temperature. In general, the acceleration method has a better chance of success for long conduction time switches while the Zeeman splitting method may be more applicable with short conduction time switches. Because the density of seed ions is very low, the technique is non-perturbing and can be applied to a variety of plasmas in addition to the POS.

The apparatus for the current density diagnostic is shown in Figure 2. This system incorporates a pulsed laser to ablate seeded material into specific regions of the switch. The laser ablation takes place a few microseconds before the switch plasma is introduced. The light emitted by the ablated material is detected by several optical fibers that are fed into a imaging monochromator with each fiber collected light from a different radial position. The spectra are recorded on an image intensified CCD camera (Princeton Instruments I-MAX ICCD). In this way we can observe, at a single time, the spectra from up to 6 locations.

Section 3
The 2D Electron Density Diagnostic

3.1 Overview.

Figure 1 shows a schematic of the Mach-Zehnder interferometer that was developed during this program. This instrument was designed to diagnose moderate to high density plasmas with phase shifts greater than 50°. The laser beam is spatially filtered, expanded, and split into two equal intensity beams by beamsplitter BS1. The beams are recombined at an angle by beamsplitter BS2 and directed onto a CCD camera. The imaging lens reduces the image size to fit onto the rectangular CCD array (8.98×7.04 mm). This lens will also correct the refractive effects of the plasma by imaging the plasma onto the CCD.
There is some flexibility to adjust the laser, and interference pattern depending on the plasma density to be probed. The laser operates at two wavelengths (1064 nm and 532 nm) with the longer wavelength twice as sensitive to index changes due to electrons. For instance, if a given path through the plasma produces 50° of phase shift with a 532 nm laser beam, then the same plasma will produce a 100° phase shift with a 1064 nm laser beam. The angle between the scene and reference beams is set by beamsplitter BS2 which has the effect of varying the amount, or frequency, of background fringes. These interference fringes are straight in the absence of plasma and are distorted when the plasma is present. The frequency of these background fringes has an impact on the type of analysis that is performed on the interferogram with the more sensitive FFT analysis requiring a very high fringe frequency. For the case where maximum sensitivity to electrons is important (low density plasma) the laser should be operated at 1064 nm with a high frequency background fringe pattern. For the case where a high density plasma needs to be probed, a 532 nm beam should be used with a low frequency background fringe pattern suitable for graphical analysis.
The viewable area of the interferometer is a function of the details of the configuration with the maximum viewable area being 4 inches. This is the nominal beam size. The characteristics of the set-up that effect the viewable area are the size of the interferometer optics (mirrors, beamsplitters) and the distance from BS2 to the CCD camera. Because

the mirrors and beamsplitters will be angled close to 45°, a certain amount of cropping will take place if these optics are smaller than 5.6 inches in diameter.
Viewable area may also be lost due to the angular difference between the scene and reference beams. To produce the background fringes, the scene and reference beams are recombined at an angle at BS2. As one moves away from BS2 the overlap area of the two beams continually decreases. Therefore, the distance from BS2 to the CCD array should be kept as short as possible to maximize the overlap area. These distances a function of the physical apparatus as well as the focal length of the imaging lens. This problem gets worse for the high background fringe frequency case where the angle between the beams is close to 0.4°. Off course, with a very large beamsplitter (BS2) the two beams may be offset on the beam splitter so they overlap exactly at the CCD array. If one uses 4 inch mirrors and beam splitters and a 300 mm focal length, the viewable area may be reduced to the 2.5-3 inch range.

3.2 Diagnostic Arrangement.

3.2.1 Laser System.

The laser system consists of a Spectra-Physics Quanta-Ray GCR-170-10 pulsed Nd:YAG laser. It operates at 10 Hz with and the wavelength can be set to either 1064 nm (fundamental) or 532 nm (doubled). An internal cavity mounted injection seeder (Spectra-Physics Model 6350) is used to ensure a single longitudinal mode in the output pulse. As we have mentioned, this greatly improves the beam spatial coherence which is important for interferometric applications. For the seeder to function properly the laser must be continuously operated at 10 Hz.
When optimally aligned, the output energy is 850 and 435 mJ at 1064 and 532 nm respectively, and the jitter is 2 ns. The beam exiting the laser is 8 mm in diameter and collimated.

3.2.2 Laser Shutter.

Since the laser must be repetitively operated, a fast laser shutter (NM Laser Products, Inc., Model #LS055S3W8) is used to pick out a single pulse at the proper time. The shutter is placed very close to the output aperture of the laser and acts as a beam dump when not in use. The shutter opens on the rising edge of a 5 V input signal and remains open as long as the input is high. Opening and closing response times are approximately 20 ms. Timing of the shutter with the laser pulse and external event will be discussed in a later section.

3.2.3 Spatial Filter.

Prior to expanding to a 4 inch beam, the laser beam is passed through a spatial filter to remove unwanted spatial modes. Such filtering improves beam uniformity and collimation. The spatial filter consists of a 500 mm focal length bi-convex lens and a 200 μm diamond pinhole inside a small vacuum chamber. The vacuum chamber is necessary to prevent air break-downs when the laser beam is focused by the lens. The beam exiting the spatial filter assembly is expanding. The spatial filter is placed immediately after the laser shutter and may be conveniently oriented by using turning mirrors to steer the laser beam. We found that placing the spatial filter parallel to the laser head via two turning mirrors allowed us to place the laser, shutter, spatial filter, and expander on a single 4×8 foot optical table.

3.2.4 Beam Expander.

The beam expander consists of a series of optics that expand the beam and re-collimate it. This is done by passing the beam through a 100 mm (nominal 4 inch) laser collimator (Newport T28-100-300). For our application we replaced the entrance objective of the collimator with a 10 mm diameter, -21 mm focal length lens fastened to the front of the collimator body. Spacing between the spatial filter and the collimator is crucial because the beam is expanding after passing through the spatial filter. The beam exiting the expander section is nearly 4 inches in diameter and well collimated if adjusted properly.

3.2.5 Interferometer Optics.

The optics that comprise the Mach-Zehnder shown in Figure 1 are a pair of mirrors, a pair of beamsplitters, and an imaging lens. The mirrors and beamsplitters are 4 inches in diameter and the lens was a 3 inch diameter achromat. The 50% beamsplitters are designed to be placed at $\sim 45°$ to the beam path and are coated for a specific wavelength. There was one set of beamsplitters for operation at 1064 nm and 532 nm.
The lens was used to image the phase object (plasma) onto the camera with the proper magnification. This lens had a broadband anti-reflection coating that could be used with both wavelengths. Refraction from the phase object is also corrected by the lens, assuming the lens diameter is large enough to catch the refracted rays. The refractive correcting power depends on the lens diameter and distance from the phase object and is proportional to the diameter of the lens divided by its distance from the phase object.

3.2.6 High-Speed CCD Camera.

The interferograms were recorded using a Princeton Instruments PentaMAX 1317K1 camera system. The CCD array measures 8.98×7.04 mm that contains a 1317×1035 pixel array. This camera has a 12-bit dynamic range and can read out a full frame in 0.33 s (5 MHz).

A small portable computer was used to control the camera functions. This was a relatively standard Pentium PC. Most often the camera was set to capture one or two frames before storing the information. The total number of frames that could be captured was a function of the available RAM of the PC. With 64 MB of RAM we could capture 18-20 frames. Other camera functions such as the resolution, type of triggering, etc. was also set with the PC.

The camera housing contained a shutter directly in front of the CCD array for general protection and to avoid overexposure. Triggering the camera was accomplished using an inverted TTL pulse and was timed to coincide with the opening of the laser shutter. Approximately 10 ms was required for the camera shutter to fully open and the amount of time the shutter remained open was controlled by the computer.

In general, the laser beam required attenuation to avoid over exposure during the recording of interferograms. This was accomplished using combination of neutral density and laser line filters that were placed very close to the CCD shutter. This effectively prevented exposure from background light as well.

3.2.7 Physical Arrangement.

The interferometer shown schematically in Figure 1 was set-up at HY-Tech Research Corporation to observe the plasma in a planar POS and on the ACE-4 facility to observe the immediate downstream region of the POS. The physical arrangements of these two systems were very different.

At HY-Tech the entire interferometer including the laser, optics, and camera, were mounted on two optical tables that straddled the vacuum chamber. This configuration is shown in Figure 3 where the dotted rectangles show the components on each respective optical table. From the standpoint of stability this was an ideal arrangement.

ACE-4 is a significantly larger apparatus where the region of interest is elevated approximately 12 feet off the ground. There is mezzanine structure surrounding the vacuum chamber windows that is far from stable. In fact, besides the floor, the most stable mounting point was the tops of the Marx tanks. Figure 4 shows the arrangement of the interferometer optics and CCD camera that was used for this machine. The laser, laser

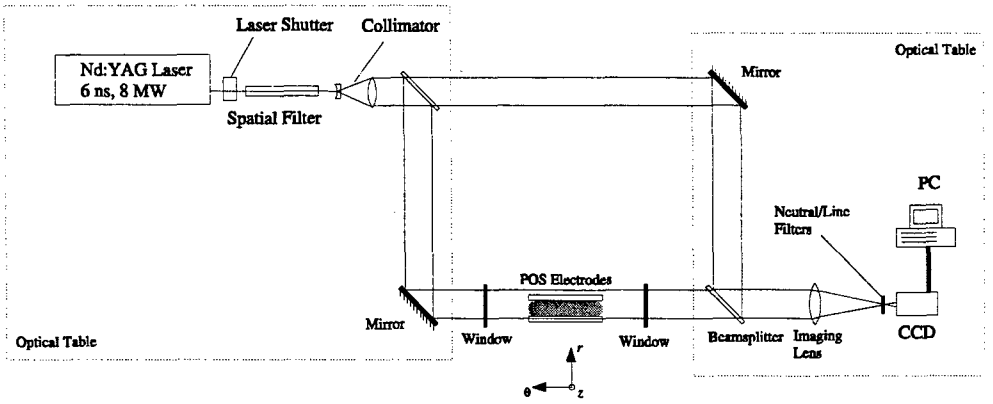

Figure 3. A schematic of the Mach-Zehnder interferometer as configured on HY-Tech's planar POS using 4 inch optics. Elements specific to the HY-Tech set up, such as the orientation of the POS electrodes and optical tables, are included.

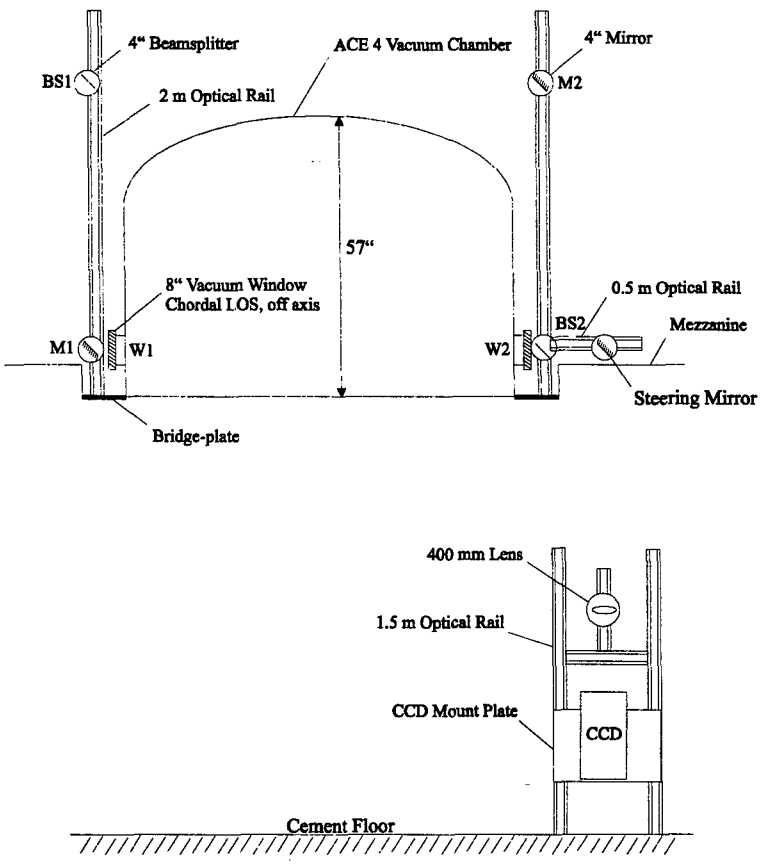

Figure 4. A schematic of the layout used for the Mach-Zehnder interferometer on ACE-4. A system of rails was used to mount the interferometer optics vertically as well as the detector optics. The laser, laser shutter, spatial filter, and collimator were mounted on an optical table (not shown).

shutter, spatial filter, and beam expander (not shown) were all mounted on a single 4×8 foot optical table that rested on one of the Marx tanks. Rails were used to mount the interferometer optics as well as the CCD camera. The interferometer rails were fastened to a flange (called the bridge-plate) on the vacuum system and the camera rail system was mounted to the cement floor. Although the camera mount system was very stable, the 1.5 m rails attached to the bridge-plate would vibrate rather easily.

3.3 Interferogram Analysis.

This section will describe the analysis of the interference pattern concentrating on the Fourier analysis of high fringe frequency interferograms. Only a brief mention of low frequency interferograms will be made as this analysis has become relatively standard and is of limited value for plasmas in the density range of interest. We will concentrate on the calculation of a 2D pattern of phase shifts from the interference pattern.
The phase shift is directly proportional to the line integral of the electron density along the path of the laser beam with the proportionality constant dependent on the wavelength. The mathematical relation for the phase shift ($\Delta\phi$) in radians is given by the following:

$$\Delta\phi = \frac{e^2\lambda}{4\pi\epsilon_o m_e c^2}\int n_e dl, \tag{1}$$

where n_e is the electron density, λ is the laser wavelength, and the integral is taken along the path of the laser beam. Inserting the values for the constants, using nanometers for the laser wavelength, centimeters for the path through the plasma, and measuring the density in units of $\times 10^{17}$ cm^{-3}, the relation becomes,

$$\Delta\phi = (0.0028)\lambda\int n_e dl. \tag{2}$$

This relationship indicates that longer wavelengths will be more sensitive to the electron density because they will produce larger phase shifts.

3.3.1 Low Frequency Interferograms.

Low frequency interferograms are interference patterns with a relatively low number of background fringes. These types of interferograms are typical of 2D interferometry measurements on plasmas for over 30 years.[14] An example of two such interferograms are shown in Figure 5 that were taken on a planar POS at HY-Tech. These types of patterns can be analyzed graphically. In the absence of plasma the background fringes are straight (part (a)). When plasma was introduced, as shown in part (b), the position of a given

(a) (b)

Figure 5. Two low background fringe frequency interferograms that were taken on HY-Tech's planar POS. Part (a) shows the straight background fringes present when there is no plasma and (b) the distorted fringes that result when plasma is present. This is most obvious near the anode (A) and cathode (K) surfaces.

fringe may be shifted from where it would normally have been. If a given fringe is shifted to the normal position of the adjacent fringe, then there is one "fringe shift" at that point. This corresponds to 360° of phase shift and half a fringe shift to 180°, and so on. If there are several, or more, fringe shifts on a given interference pattern, then a simple graphical analysis can provide reasonable resolution. However, graphical techniques applied to situations where the maximum shift is less than one fringe are inadequate because even the best graphical techniques can only resolve 1/10 of a fringe.

One serious limitation of the graphical analysis is that there must be a reference region on the interference pattern where there is no phase distortion. Furthermore, this region must be large enough to extrapolate undistorted background fringes for the purpose of calculating the fringe shifts in two dimensions.

Low frequency interferograms are also useful because high density regions can be detected by inspection. The interference pattern shown in Figure 5(b) is a good example of this where significant bending of the fringes can be observed near the electrode surfaces indicating high electron densities in those regions.

3.3.2 High Frequency Interferograms.

Interferograms with an imposed high frequency background fringe pattern can be analyzed via a Fourier transform technique to significantly improve the phase resolution.[3] An

essential requirement for the implementation of this technique is that the interference pattern must be stored digitally so fast Fourier transform (FFT) routines can be used on the data. This method is the spatial analogue to heterodyne interferometry where the background fringe frequency acts as the carrier frequency in the transformed, or Fourier, space. How high the fringe frequency needs to be depends somewhat on the quality of the interferogram with regards to uniformity of the laser beam. The safest way to set the fringe pattern is to make it as large as possible so there is one fringe for every 3 or 4 pixels on the CCD detector.

This technique has a number of advantages in addition to the improved phase sensitivity. The two most important are the speed at which the phase distribution can be obtained and the lack of a large reference region. The process of determining the phase distribution is essentially fully automated as one simply needs to execute a few simple programs. One also does not need a reference region to connect all the fringes from an undistorted region. Using this method one only needs a small area of the interferogram where the electron density is at, or near, zero. The calculated phase in this region can then be defined as zero density and all other areas can be referenced to this zero.

The FFT Method

With the advent of powerful computers and high spatial resolution CCD cameras, the analysis of interferograms using Fourier transforms has become quite common.[3, 15, 16] This method has the advantage of being fast and accurate, with reported resolutions of 1/50 of a fringe ($\sim 7°$), and results can be obtained within a few minutes of the shot.

To effectively get phase information using this method, a large amount of background fringes must be added to the interferogram to increase the separation of the lobes in frequency space. Our goal is to introduce one background fringe for every 3 or 4 pixels on the CCD array. Under normal viewing these interferograms look unintelligible, however the FFT shows well defined peaks suitable for the analysis shown below. Figure 6(a) shows the raw intensity data from one line of an interferogram while part (b) shows its Fourier transform using a simple 1D FFT routine. In this case there were between 3 and 4 pixels per fringe. Either lobe in the transform located near the frequencies ± 0.35 Hz contains all the phase information for that line of data. If the background frequency was not high enough then the lobes at $\pm f_o$ would overlap the lobe centered near zero frequency and it would be impossible to extract the desired phase information.

The method is outlined as follows. The intensity pattern of an interferogram ($x - y$ plane)

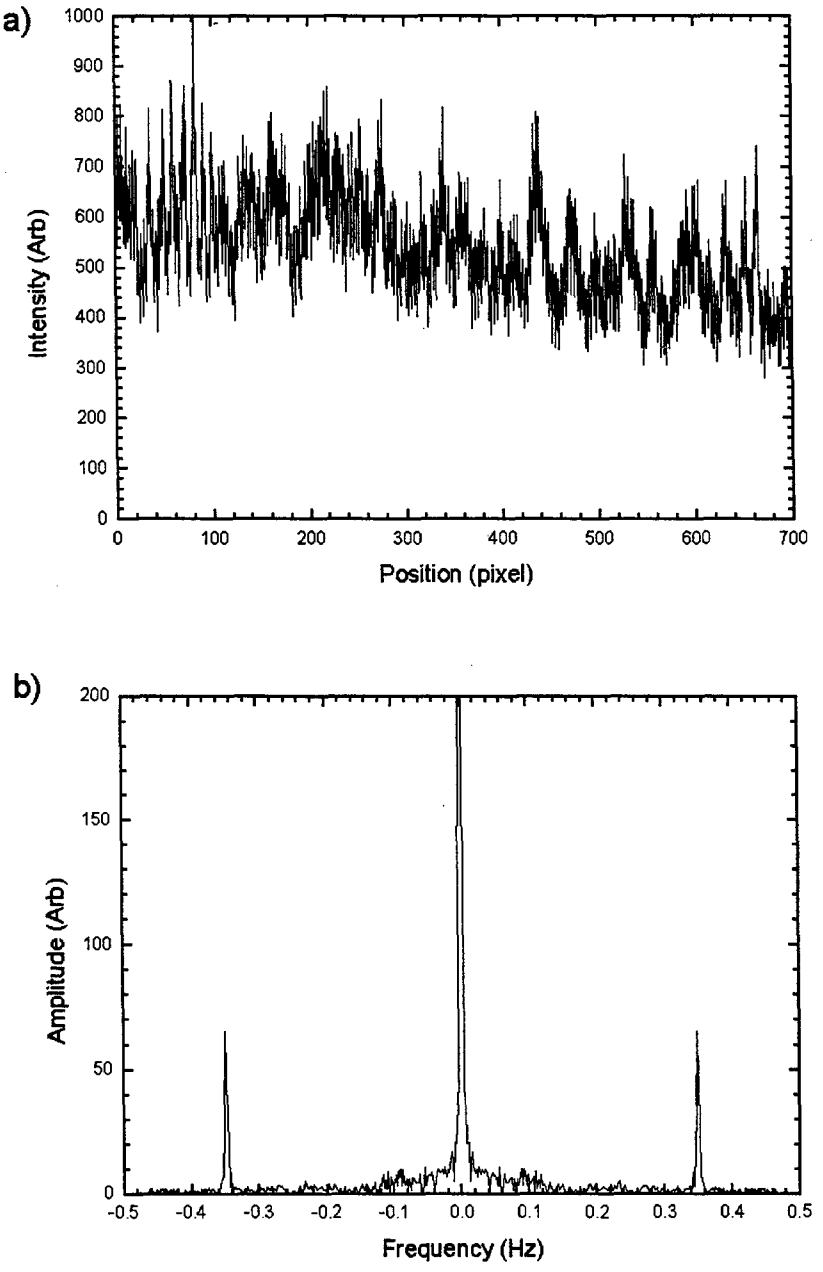

Figure 6. Part (a) shows the intensity recorded by the CCD camera for one line of a high frequency test interferogram. Part (b) show its FFT with well defined peaks at 0, f_o, and $-f_o$.

can be represented by the following equation,

$$g(x,y) \;=\; a(x,y) \;+\; b(x,y)\cos\left[2\pi f_o x + \phi(x,y)\right], \tag{3}$$

where $g(x,y)$ is the light intensity, $a(x,y)$ and $b(x,y)$ are irradiance variations, $\phi(x,y)$ is the phase of the wavefront, and f_o is the spatial carrier frequency. The term $2\pi f_o x$ produces the background fringes, and for simplicity we have taken this to be only in the x-direction. In general, the background fringe frequency will have both x and y components and the background fringe phase term would become $2\pi(f_x x \;+\; f_y y)$. Equation (3) can be expressed in exponential notation as the following,

$$g(x,y) \;=\; a(x,y) \;+\; c(x,y)\exp\left[2\pi f_o x\right] \;+\; c^*(x,y)\exp\left[-2\pi f_o x\right], \tag{4}$$

where

$$c(x,y) \;=\; (1/2)b(x,y)\exp\left[i\phi(x,y)\right]. \tag{5}$$

The Fourier transform of the x-coordinate yields,

$$G(f,y) \;=\; A(f,y) \;+\; C(f-f_o,y) \;+\; C^*(f+f_o,y). \tag{6}$$

If f_o is made large enough, so it is much greater than the spatial variations in $a(x,y)$, $b(x,y)$, and $\phi(x,y)$, then $G(f,y)$ is a trimodal function with well defined peaks at 0, f_o, and $-f_o$ as shown in Figure 6(b). By using a filter in frequency space centered at f_o, $C(f-f_o,y)$ can be isolated from the remainder of the transform. The full phase expression $(2\pi f_o x + \phi(x,y))$ can be recovered by taking the inverse transform of $C(f-f_o,y)$, and calculating the inverse tangent of the ratio of its real and imaginary parts,

$$2\pi f_o x + \phi(x,y) \;=\; \tan^{-1}\left[Re(IT)/Im(IT)\right], \tag{7}$$

where IT represents the inverse transform of $C(f-f_o,y)$.
There are a number of options available to eliminate the $2\pi f_o x$ term and determine the phase $\phi(x,y)$. One method has the function $C(f-f_o,y)$ shifted to the origin in frequency space after notch filtering around f_o before the inverse transform is taken. However, since frequency space is discrete due to the discrete nature of the FFT, we found that this method lead to unacceptable errors unless f_o was an exact multiple of the frequency spacing. We have therefore devised an alternative method where the phase term involving the carrier frequency is subtracted off after the inverse transform is performed. For this to work the carrier frequency must be known, or calculated independently.

Determining f_o

The carrier frequency is determined quite accurately from interferograms with no, or a small amount, of phase distortion. These interferograms are typically taken just before the plasma event. Alternatively, a portion of the interferogram where there is little or no distortion may be used. For both cases the assumption is that $\phi(x, y)$ is either zero or very small. Then, the analysis above will yield a phase distribution that is essentially an inclined plane, ie. the $2\pi(f_x x + f_y y)$ term. A linear fit to the inclined plane can be used to determine both components of the carrier frequency.

3.3.3 Analysis using Two Exposures.

We have developed a double interferogram method to improve the overall sensitivity of the instrument. This became a necessity because the Mach-Zehnder arrangement uses distinct optics for the reference and scene arms, ie. mirrors M1 and M2. Even though the FFT method is accurate to 1/50 of a fringe, the optics will limit the sensitivity of a given interferogram because they are flat only to $\lambda/10$. As a result we expect variations on a single interferogram with no plasma to be at least 40°. We will refer to interferograms taken with no phase object as null interferograms. In practice, the variation observed on null holograms was higher because the imaging lens caused additional distortion. Figure 7 shows the 2D phase map of a null interferogram in part (a) and a histogram of the distribution of phases over the entire image in part (b). The phase distribution shown in Figure 7 is due to differences in phase distortions introduced by the scene and reference arm optics as well as lens distortions. We will refer to such a distribution as the background phase.

If we assume that the optical system is stable, or at least stable over the time it takes to record two interferograms, then the phase distortions due to the optics will be the same on two successive interferograms, ie. the background phases are the same. If one of the interferograms also includes distortion due to plasma, then subtracting the two yields the net phase shift due only to plasma. In practice the best accuracy is obtained when the background interferogram, or null interferogram, and the measurement interferogram are taken as close together in time as possible. This reduces the possibility that environmental effects will effect the background phase between exposures. In our case we can capture two interferograms with a 0.5 sec interval, the limitation being the speed of the CCD camera. It is conceivable that with a faster camera we could capture two interferograms in 0.1 sec. The double exposure method also solves the problem of calculating the carrier frequency because the null interferogram can be used for this. These frequencies can then be applied

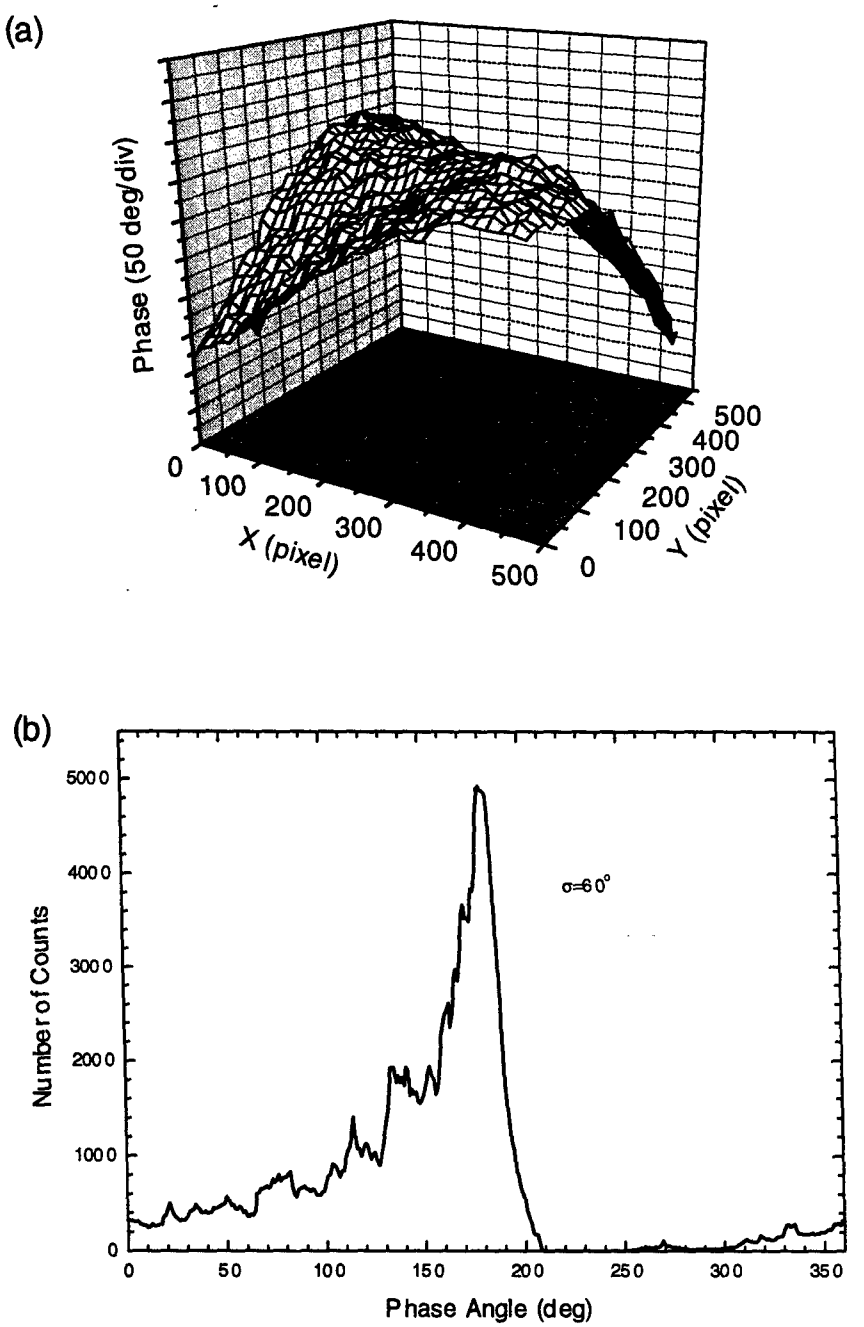

Figure 7. Part (a) shows the 2D phase distribution from an single interferogram with no plasma present and part (b) is a histogram of this distribution.

to the second interferogram with plasma.

3.3.4 Tests of the Double Exposure Method.

If the interferometer were perfectly stable, as well as the environment where it resides, then the subtraction of the phase distributions from two null interferograms would produce errors comparable to the resolution of the FFT method. We would expect that, in the best case, this distribution would deviate from the average by $\pm 7°$ or 1/50 of a fringe. Additional errors could result from a number of sources, such as the laser wavefront changing between pulses, subtle shifts in the position of the optics, thermal motion of the optics, or possible air motion between exposures.
By capturing a series of null interferograms we can determine the sensitivity of the system. Typically we would capture a series of 10 interferograms and analyze successive pairs to determine the measurement sensitivity. A convenient way to quantify this is to plot a histogram of the phase distribution obtained from the subtraction of two test phase maps. For the null interferogram tests we will report in the next two sections the laser was operated at 1064 nm. This is by far the most useful setting where accuracy is concerned. An anomalous behavior was observed during test runs at 532 nm where large errors were observed due to a shift in the background frequency between exposures. The errors were three to five times larger than at 1064 nm. To this date we do not have a satisfactory explanation for these observations and our recommendation is that for cases where high phase sensitivity is required the 1064 nm wavelength be used exclusively.

Null Tests at HY-Tech

Figure 8 shows the phase distribution in part (a) and the histogram for that distribution in part (b) from a the subtraction of two null interferograms. One of these interferograms was the one displayed in Figure 7. These plots, when compared to Figure 7, illustrate the gain in accuracy from the double interferogram method. The distribution in part (b) is very close to a Gaussian with an uncertainty of $\pm 7.8°$. A portion of this uncertainty is due to small changes in the carrier frequency between exposures, which is assumed to stay constant. Many such tests were performed with distributions that looked similar to that shown in Figure 8(b). For 25 pairs of interferograms the uncertainties averaged $7.9 \pm 3.9°$.

Null Tests on the ACE-4 Interferometer

Sequences of null interferograms were also captured when the interferometer was set-up on the ACE-4 facility at Maxwell Technologies. The results from these tests showed that the

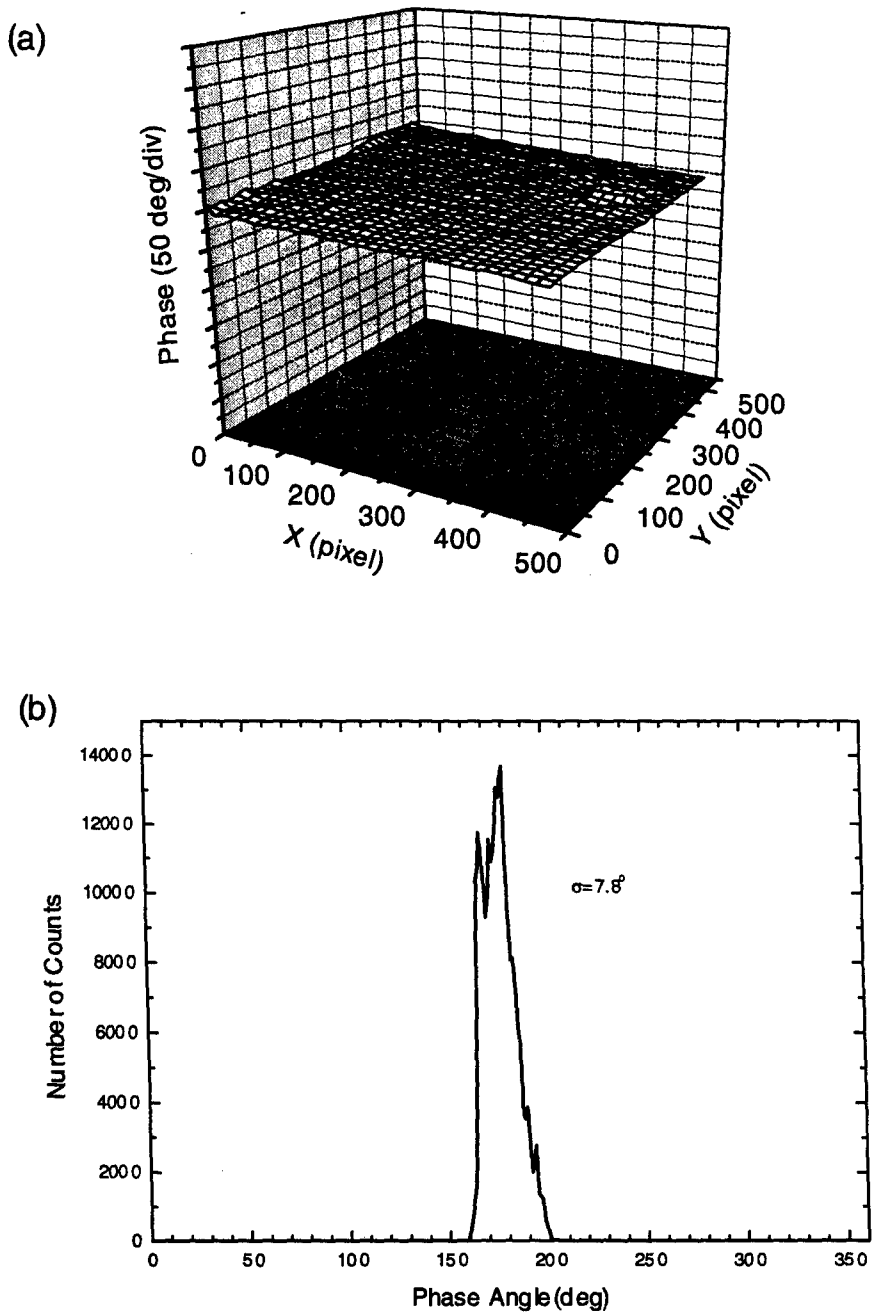

Figure 8. The 2D phase distribution (a) and histogram (b) obtained from the subtraction of two null interferograms one of which was the interferogram displayed in Figure 7.

distributions were wider with an average over nine pairs of 9.8±1.9°. This increase was most likely due to the mounting system used on ACE-4 where 1.5 meter rails were used to mount the interferometer optics in place of the optical tables used at HY-Tech.

3.3.5 Analysis Software.

Computer programs were developed at HY-Tech to analyze 2D interference patterns. Two programs were developed; one (ASC2BIN) that converts intensity data files to binary and another (INTER_ANAL) that performs the calculations required to determine the 2D phase distribution. A standard binary format was defined for the intensity files to reduce their size and speed up loading into INTER_ANAL. The INTER_ANAL routine performs the bulk of the functions including the calculation of carrier frequency components from background interferograms and subtraction of background phase distributions. A 2D FFT routine is an integral part of this analysis that is used to calculate the carrier frequency components as well as the phase via equation (7). Due to the nature of the 2D FFTs the analysis is limited to rectangular regions.

To fully analyze an interferogram the following steps are performed on a pair of interferograms:

1. The approximate carrier frequency components are calculated from a background interferogram by counting fringe maxima.
2. The 2D FFT is calculated for the background interferogram and is filtered around the maximum amplitude of the FFT near the approximate frequency.
3. The inverse transform is performed on the filtered data and phase calculated via equation (7).
4. The exact frequencies are calculated by a linear fit to an inclined phase plane.
5. The 2D FFT is calculated for the second interferogram with phase distortion and filtered around the same point in frequency space as in step (2).
6. The inverse transform is performed on the filtered data.
7. The phase due to the exact carrier frequency (step (4)) is subtracted off.

The filter that is used on the transformed data is a simple 2D notch where the immediate area around the peak in the FFT is unchanged and the remainder of the distribution is set to zero.

Our algorithms were checked by using fictitious interferograms created numerically with small phase distortions and simulated irradiance variations. An example of such a test phase distribution is shown in Figure 9; it is asymmetric and has a peak phase shift of 22°. A simulated intensity pattern was created based on this phase distribution using equation

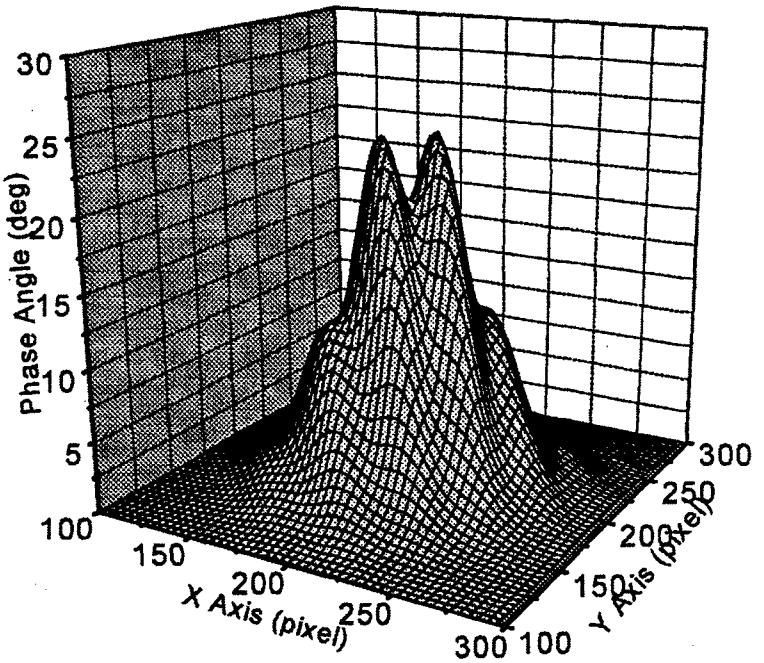

Figure 9. The phase distribution that was created numerically to test the analysis software.

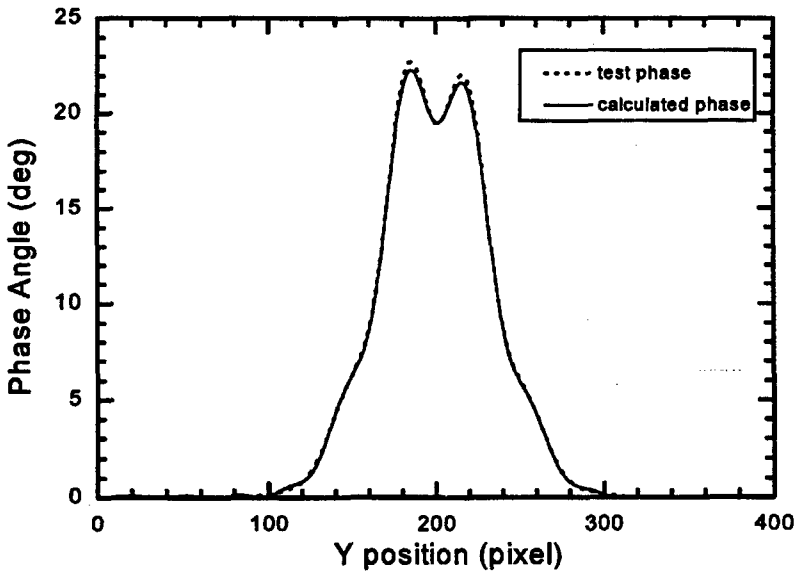

Figure 10. A comparison of the test phase and calculated phase for a single line at x=200. The difference is only a few percent at its maximum point.

(3) with a background fringe pattern having $f_x = 0.33$ Hz and $f_y = 0.21$ Hz. The dimensions of the test interferogram were 400 by 400 pixels. A simple, smoothly varying irradiance function that peaks in the center and decreases toward the edges of the interferogram was used. The effects of random noise were not included. After processing the simulated interferogram, the calculated phase is nearly identical to the test phase shown in Figure 9. A comparison of the input test phase and the calculated phase is shown in Figure 10 for a slice through the distribution at x=200.

3.4 Operation of the Interferometer.

This section will describe the operation of the interferometer in a pulsed power experimental situation. This will include the shielding of sensitive electronic equipment, synchronizing the diagnostic with an experimental event, and tests on POS plasmas at HY-Tech and Maxwell Technologies. We will also make some comments with regard to increasing the viewable area.

3.4.1 Electromagnetic Shielding.

As is the case in most pulsed power experiments equipment with sensitive electronic components must be shielded from the electromagnetic noise that is generated. This noise may cause malfunctions in various components, such as laser pre-triggering that was observed at HY-Tech during initial testing. The noise may couple to the equipment either through the air or via the power grid. The laser, laser power supply, portable computer, CCD camera, etc. were all shielded to prevent contamination from both avenues.

All the electronic components of the interferometer were enclosed in aluminum boxes for shielding purposes. We constructed separate boxes for the laser, laser power supply, CCD camera, and computer. Fans were installed in the laser, laser power supply, and camera boxes to facilitate air cooling of these components. Cables between the laser and laser power supply were passed through an aluminum hose, which allowed the two boxes to act as one large Faraday cage. The laser box is generally grounded at the optic table it rests on, and if possible, the laser power supply box should be isolated from ground to prevent ground loops. In a similar manner, an aluminum hose forms a conduit for the connection between the CCD camera and computer.

The power lines for all components are filtered using commercially available RFI/EMI filters.

3.4.2 Synchronization.

When using the interferometer to make measurements of a transient event, such as in a POS, the laser pulse must be synchronized with the external event. We refer here to the second laser pulse that is used to measure the phase of the plasma. This must be done with a high degree of accuracy because the timing of the laser pulse determines the operating window of the diagnostic. It is desirable to be able to control this to within 10 ns for long conduction time switches. The synchronization of the plasma and the laser pulse is complicated by the operation of the injection seeder which requires the laser to be continuously operating at 10 Hz.

We developed two options to allow us to synchronize the two events. The first option uses the output of the laser to trigger the pulsed power experiment, and the second option triggers the laser off a timing event from the experiment. The first option is most desirable because it assures reliable laser operation and has been used in actual experiments at HY-Tech and Maxwell Technologies. The second option has been tested.

Using the Laser as a Timing Device

The electronics that were developed to use the laser as a timing device is shown in Figure 11 and the associated timing diagram in Figure 12. This method uses the flashlamp sync and Q-switch sync output of the laser as inputs to a series of 74LS123 multivibrator chips or "one shots". These sync signals are trains of 10 Hz square wave pulses that are 5 ms in duration. The rising edge of each square wave corresponds to the initiation of the flashlamp and Q-switch electrical circuits and are delayed by the pump time of the laser cavity ~ 175 μs. The user initiates the sequence with a 22 volt input pulse that enables the multivibrator circuit. Upon the arrival of the next Q-switch sync pulse, the laser and camera shutters are opened 20 ms later and held open for 150 ms. As a result, both shutters are open for the next laser pulse only. This pulse would be used for the background interferogram. The shutters are opened again 500 ms later and an additional pulse is sent to a digital delay generator (DDG) on the rising edge of the flashlamp sync signal. The laser pulse will be emitted approximately 175 μs later and the DDG must be set to trigger the experiment at the appropriate time.

Although the delay between the rising edge of the flashlamp sync and the laser pulse is variable and set by the user, once it is adjusted the jitter is very low at only a few ns. Therefore, if the jitter in the pulsed power experiment is low then the interferometer can be timed quite accurately.

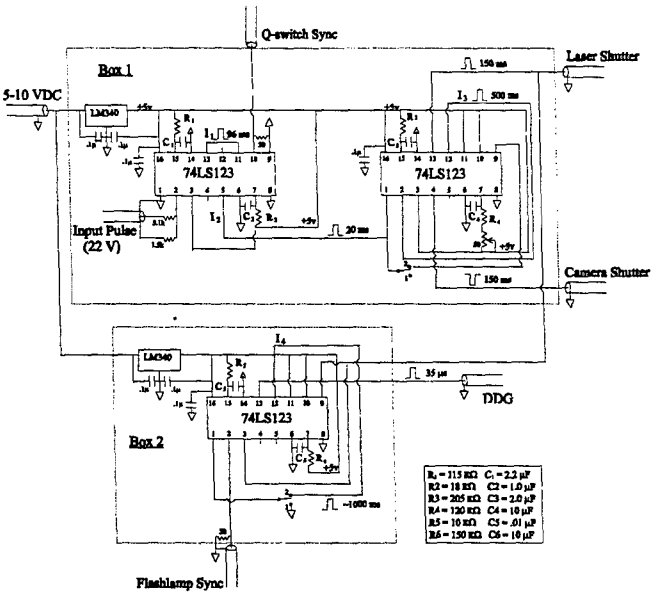

Figure 11. A schematic of the circuit used to control the laser shutter, camera shutter, and external event via the DDG pulse. The Q-switch SYNC, flashlamp SYNC, and 22 V pulse are used as inputs.

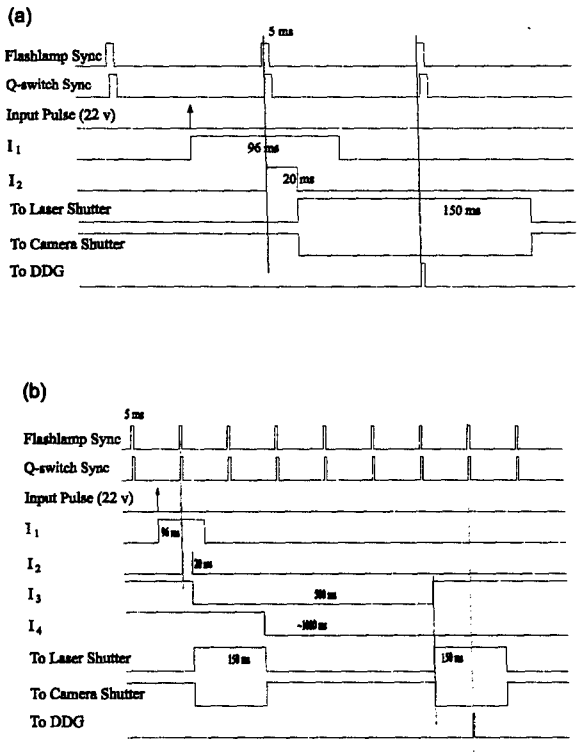

Figure 12. Timing diagrams for single pulse (a) and double pulse (b) operation. All signals are TTL level.

Timing off the Experiment

For situations where the jitter in the pulsed power machine is unacceptably large or, a 175 μs window is not long enough to initiate the pulsed power event, an alternative laser triggering scheme was developed. This second option uses a signal from the pulsed power triggering scheme, to initiate the laser discharge. Figure 13 shows the electrical circuit that is used for this approach. The process involves continually triggering the laser Q-switch at 10 Hz using the multivibrator circuit. The laser is set to accept an external Q-switch trigger and the flashlamp sync signal is used as an input. As shown in Figure 13 the external trigger from the pulsed power experiment is mixed with the 10 Hz Q-switch trigger. The only caveat is that the external signal must come a few microseconds before the normal Q-switch pulse. When this occurs the external signal will trigger the laser and the following pulse from the multivibrator circuit will do nothing. In this way the timing of a single laser pulse can be controlled with a fully functioning seeder. The slightly shorter flashlamp delay will effect the output power, but only by a small amount. With the scheme the laser shutter and CCD camera shutter need to be externally trigger using a DDG at the appropriate time.

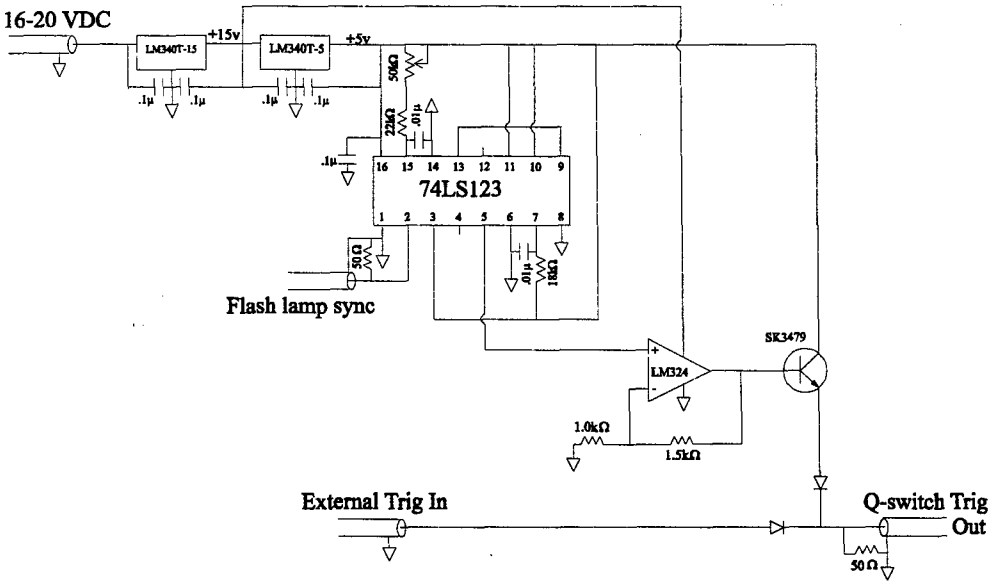

Figure 13. Circuit schematic for triggering the laser with an external signal.

3.4.3 Interferometer Measurements on the Planar POS.

The planar plasma opening switch at HY-Tech was used to test the interferometer. This allowed us to use the FFT based analysis on a real phase object, and test the synchronization method and shielding equipment. Using the arrangement shown in Figure 3 we captured a series of interferograms at various times during the conduction phase. The area probed by the interferometer over the course of many shots is shown in Figure 14 where the scene laser beam was directed perpendicular to the plane of the drawing (y-direction). On any one shot, an axial length of 3.5 cm could be viewed.

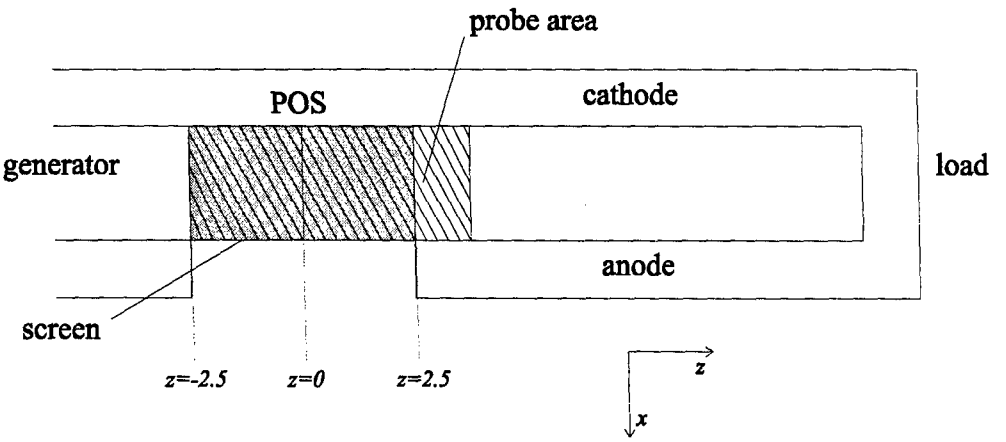

Figure 14. Scaled drawing showing the probe region used on the planar POS. Multiple shots were used to view the entire area shown because a 3.5 cm axial region could be viewed on a single shot.

Most of the interferograms were taken in the high frequency fringe mode so full 2D analysis was obtained. Figure 15 shows three different interferograms displayed as 2D contour plots with the anode and cathode defined as x=0 and x=2.5 cm respectively and the load edge of the switch at z=2.5 cm. In this series of plots we can see a density front propagate toward the load and thinning closer to the cathode. We can also see very large densities on each electrode surface including regions downstream of the load edge of the switch.

3.4.4 Field Measurements on ACE-4.

The interferometer was also used to probe the downstream switch region on ACE-4 with the set up shown in Figure 4. On this machine both low and high frequency interferograms were taken. In this particular region there is, in general, a much smaller phase shift because we are not probing the switch region directly. Heterodyne interferometry had measured phase shifts in the 60° range which corresponds to about 100° at 1064 nm. As a

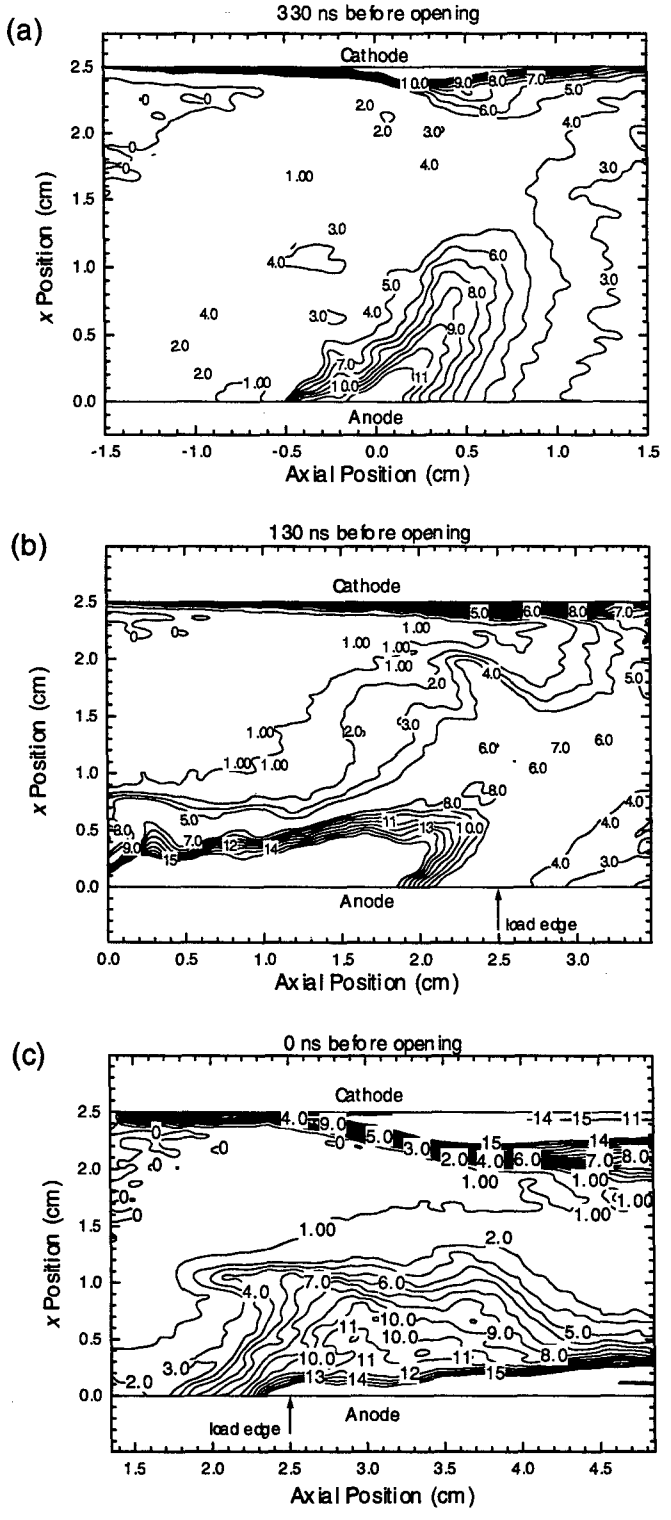

Figure 15. Contour plots of the interferometry data taken on the planar POS at three different times during the conduction phase where each contour line is separated by 1×10^{15} cm^{-3}. This set of data illustrates bulk plasma motion toward the load and thinning nearest the cathode. Note each plot has slightly different axial limits.

result we did not expect to see a large effect except near the electrodes. As Figure 16 shows significant fringe bending was only seen near the cathode which is best illustrated using a low frequency interferogram.

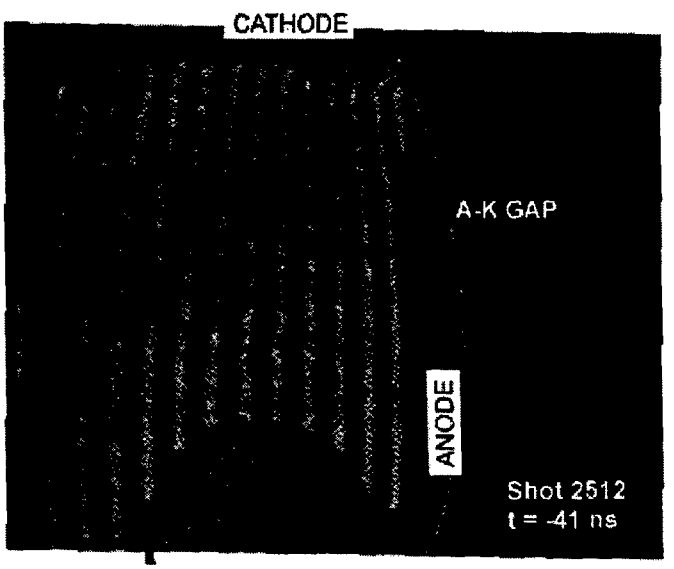

Figure 16. A low frequency interferogram taken on ACE-4 where large densities on the cathode surface can be observed. This interferogram was taken 41 ns before opening.

Section 4
The Magnetic Field Diagnostic

4.1 Overview.

This aspect of the program was designed to develop a diagnostic to measure the two dimensional current density distribution in a POS. While the current is impossible to measure directly, it can be calculated from Ampere's Law if the magnetic field distribution is known. Thus, our diagnostic techniques have concentrated on determining this quantity. The magnetic field diagnostic is based on the observation of line spectra from material that is introduced externally into the plasma in small quantities. We refer to this material as seeded material. The seed material must be appropriately chosen so the transitions of interest exist and are not normally present in the switch plasma. This last requirement precludes one from injected carbon for switch operated with cable guns or flashboards. This method allows one to perform localized measurements to within the dimensions of the seeded column. Similar investigations of plasma properties using seeded materials have been reported by Y. Maron and co-workers.[12, 13, 10]

We have investigated various seeding techniques using laser ablation to introduce a column of material in the switch just prior to the introduction of plasma. The ablated plume was characterized to determine its spatial extent using spectroscopic observations.

To map the two dimensional distribution of the field we have set up a multi-chord viewing system so the field at several locations can be measured simultaneously. This apparatus involves a series of optical fibers, an astigmatically corrected high resolution monochromator, and a two dimensional intensified CCD camera (ICCD camera). This apparatus has the capability to record the spectra from each location at a given point in time.

The diagnostic is operated by forming a column of seeded material a few microseconds before the switch plasma is introduced. The interaction of the plasma with the seed material may ionized and/or excite these atoms so the transitions of interest can be observed. This column must by perpendicular to the magnetic field, and in cylindrical geometry is oriented along the radial direction. The light collection system is then set to

view the plasma along the axial direction at various radial positions. Since we only view emission from seed ions, the measurement is localized in the z-direction by the width of the seeded column and the r-direction by the light collection system. During the conduction phase of the switch we can collect light from several radial positions simultaneously determined by the gate time of the ICCD camera.

Two different techniques were investigated for measuring the magnetic field distribution; one that involved measuring the Zeeman splitting and the other that measures the ion velocity. The techniques differ in the type of analysis and the requirements of the seed material. Depending on the type of switch, or the characteristics of the switch plasma, one technique may be more applicable then the other. For instance, the Zeeman technique requires seeded ions (or neutrals) that are heavy to reduce Doppler broadening. This situation is more likely to occur in lower density switch plasmas more characteristic of short conduction time switches such as on DM1. On higher density switch plasmas, such as ACE-4, the ion acceleration method may be more applicable.

It is important to characterize the unseeded plasma to determine the time history of both the electron density and the electron temperature. The electron density may be obtained from interferometry while a determination of the electron temperature must involve spectroscopic observations. Time histories of various carbon lines are very useful in this regard. These characteristics can be used with time dependent CRE models to predict the existence of ion charge states and emission levels. Such knowledge will help determine which analysis method (Zeeman or ion velocity) is most appropriate for a given switch. Furthermore, it will also help choose the specific seed material.

At the conclusion of this program a successful field measurement had not been completed due to limited resources. We have, however, completed the analysis required to make the measurement on HY-Tech's planar switch. This includes a characterization of the ablation methods and the switch plasma. We will offer a prescription for completing a field measurement on other switches.

4.1.1 Zeeman Splitting Analysis

The Zeeman splitting refers to the splitting of the energy levels of an element according to the value of the z-component of the total angular momentum vector. This splitting is linearly proportional to the magnetic filed with a relationship given by the following equation:

$$\Delta\lambda = \frac{-\lambda_o^2}{hc}\mu_B B[g(2)m_j(2) - g(1)m_j(1)] \tag{8}$$

where B is the magnetic field, λ_o is the unshifted transition wavelength, μ_B is the Bohr magneton, $g(i)$ is the Lande factor for the i^{th} level, and $m_j(i)$ is the quantum number associated with the z-component of the total angular momentum vector. The σ component is characterized by $\Delta m_j = -1$ while the π component has $\Delta m_j = 0$. Both of these components can be observed perpendicular to the magnetic field with different orthogonal polarizations with respect to the field direction. Therefore, a measurement of this splitting can be used to directly calculate the magnetic field if a acceptable transition is observable.

4.1.2 Ion Velocity Analysis

A measurement of the magnetic field using the Zeeman effect may fail in some areas of the switch due to an insufficient level population, or an overwhelming Doppler broadening. This is more likely to occur in longer conduction time, higher plasma density switches. In these cases the field can still be measured by measuring the ion velocity of the seeded elements. The ion directed velocities can be determined from the Doppler shift of the line emission. If the electron density is also known we can use the ion equation of motion in the plasma to unfold the magnetic field.[12]

By measuring the time history and axial distribution of the ion velocity we can deduce the magnetic field under the assumption that the Hall electric field accelerates the ions. The generalized Ohm's law equation under the assumption of insignificant resistivity, immobile ions, and negligible pressure gradients gives the following relationship between the electric and magnetic fields:

$$\mathbf{E} = \frac{-\mathbf{v}_e \times \mathbf{B}}{c}, \tag{9}$$

where $\mathbf{v}_e$ is the electron fluid velocity. The equation of motion for the seeded ion in the z-direction is:

$$M_i \frac{dv_i}{dt} = Z_i e E_z, \tag{10}$$

where M_i is the mass of the ion and Z_i the ion charge. For the case of a cylindrical POS, $\mathbf{v}_e$ is in the radial direction and remembering that $\mathbf{B}$ only has a θ component and varies in the z direction, we can express $\mathbf{v}_e$ as:

$$v_e = \frac{J}{e n_e} = \frac{c}{4\pi e n_e} \frac{\partial B_\theta}{\partial z}, \tag{11}$$

where J is the current density, n_e the electron density, and we have used Ampere's law. Now the equation for E_z becomes:

$$E_z = \frac{1}{8\pi e n_e} \frac{\partial B_\theta^2}{\partial z}, \tag{12}$$

where we have made use of the relation

$$\frac{\partial B_\theta}{\partial z} \times \mathbf{B} = \frac{1}{2}\frac{\partial B_\theta^2}{\partial z}. \tag{13}$$

We can put this together to obtain a relation between the ion acceleration and the gradient in B_θ^2:

$$\frac{dv_i}{dt} = \frac{Z_i}{8\pi M_i n_e}\frac{\partial B_\theta^2}{\partial z}. \tag{14}$$

In practice one actually measures the ion velocity as a function of time to obtain the acceleration. To obtain the gradient in B^2 the ion velocity must be measured as a function of z as well.

4.2 Diagnostic Arrangement.

There are two distinct systems that comprise the physical apparatus for the current density diagnostic as shown in Figure 2. These are the laser ablation system and the light collection system. The laser ablation system is used for seeding the plasma with a column of material. It consists of a high power, short pulsed laser, a focusing lens, and a solid target or glass slide with a thin film. The light collection/detection system detects the optical emission from the seeded material. The major components of this system are:

1. An optical probe array, consisting lenses coupled to 10 m UV grade optical fibers with a spatial resolution of ~3 mm.

2. A McPherson 0.67 m imaging monochromator with a 2400 g/mm grating; linear dispersion ~4 Å/mm.

3. A Princeton Instruments I-MAX intensified CCD (ICCD) camera with a 512 x 512, 16-bit format.

4.2.1 Ablation System

A more detailed view of the ablation system is shown in Figure 17 where we show the arrangement used to ablate material from either a glass slide or a solid target. Various short pulsed lasers (10-50 ns) with energies in the range of 0.5-1 J may be used for ablating material into the POS plasma. During our tests we used a 0.5 J, 30 ns pulsed ruby laser, but the YAG laser that is used for the interferometry can also be used as an ablator. A lens must also be used to focus the laser beam so adequate power densities are achieved. Although we have shown the lens outside the vacuum system, it may be inside as well.

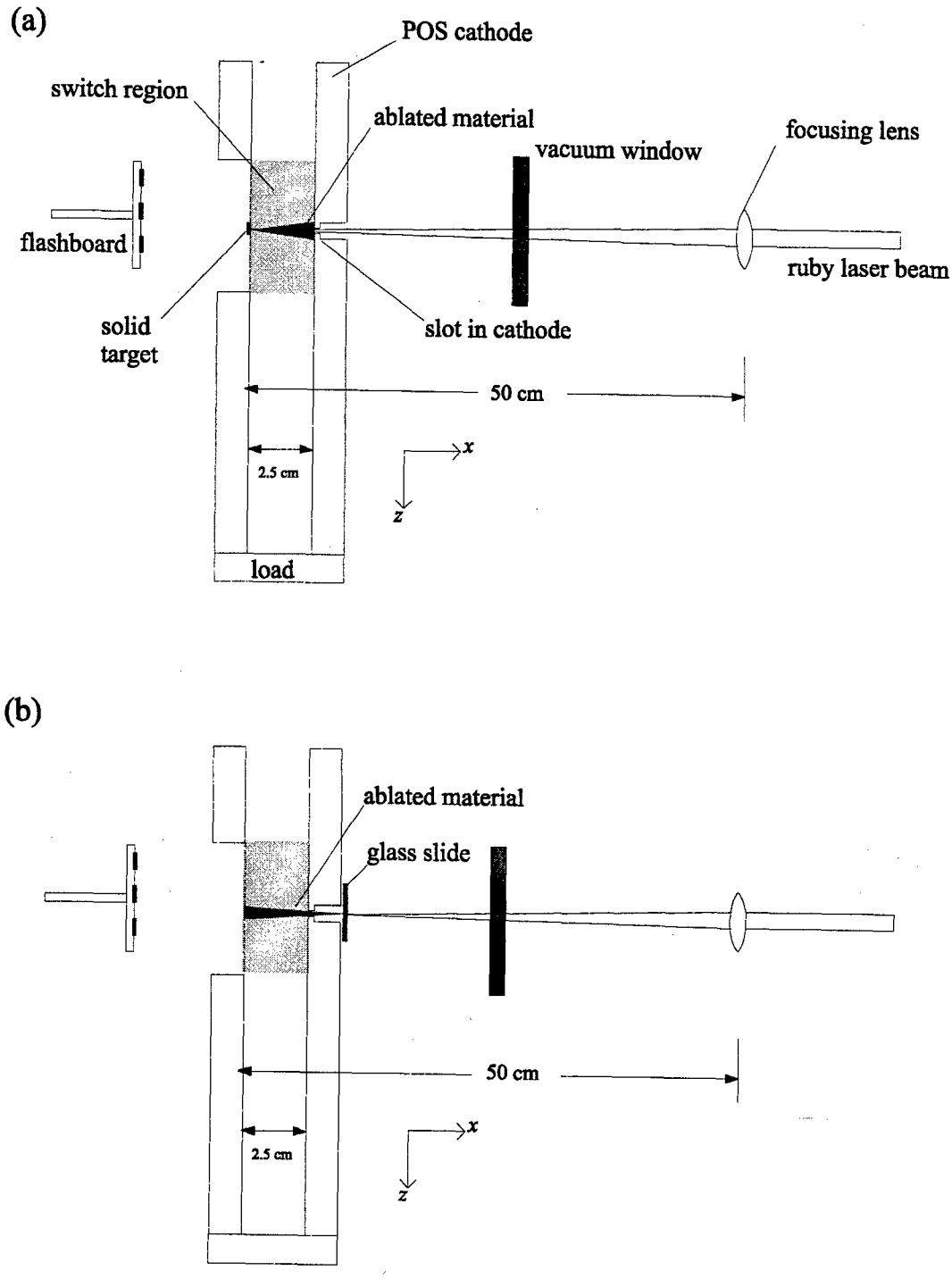

Figure 17. The ablation apparatus used for introducing seeded material into the POS. Two methods are illustrated; (a) uses a solid target embedded in the anode and (b) uses a glass slide with a thin film of material on the side facing the switch.

Depending on the material one wishes to seed, either the film or solid target method may be more applicable. The film/glass slide method (Figure 17(b)) should be used whenever possible because apertures can be used to collimate the plume and improve spatial resolution. This is not possible using the solid target method. However, some materials are very difficult to evaporate onto films and the solid target method is the only practical alternative.

For the solid targets, which are mounted in the anode as shown, we have used hot pressed boron chunks, or boron and LiF powder mixed with epoxy. These material were used for injection of boron and lithium respectively. In this scheme the ablated plume blows off the surface into the POS gap.

We have also successfully experimented with ablating thin films off glass slides. Typically the film thickness is 2-4 μm with the slide located outside the cathode behind a slot. The laser is directed through the glass and the plume blows off the glass surface into the POS gap. The major advantage of the slide method is that it is very easy to collimate the plume via apertures in the cathode. The disadvantage of the thin film method is that some materials are very difficult to evaporate onto glass. Boron is one example.

We also breifly explored the possiblity of using gas injection for seeding the plasma. However, cosiderably more effort on the design of a collimating gas nozzle is required to achieve adequate spatial resolution. Ne would be a good choice for such an injection scheme.

4.2.2 Light Collection and Detection System

The arrangement of these items was shown schematically in Figure 2. A series of optical fibers and lenses is used to bring light from various radial locations to the input of an imaging spectrometer. The six fiber system that we have fabricated has a radial spatial resolution of 3 mm and would be oriented along the direction of the ablated column (radial direction).

These fibers are lined up along the input slit of the spectrometer so at the output plane the various spectra would be displaced vertically and can be recorded with a 2D detector such as the ICCD camera. Time resolution is obtained by gating the camera with gates as small as 5 ns possible. We have purchased a Princeton Instruments I-MAX ICCD camera to function as the detector.

4.3 Characterization of the Seeded Plume.

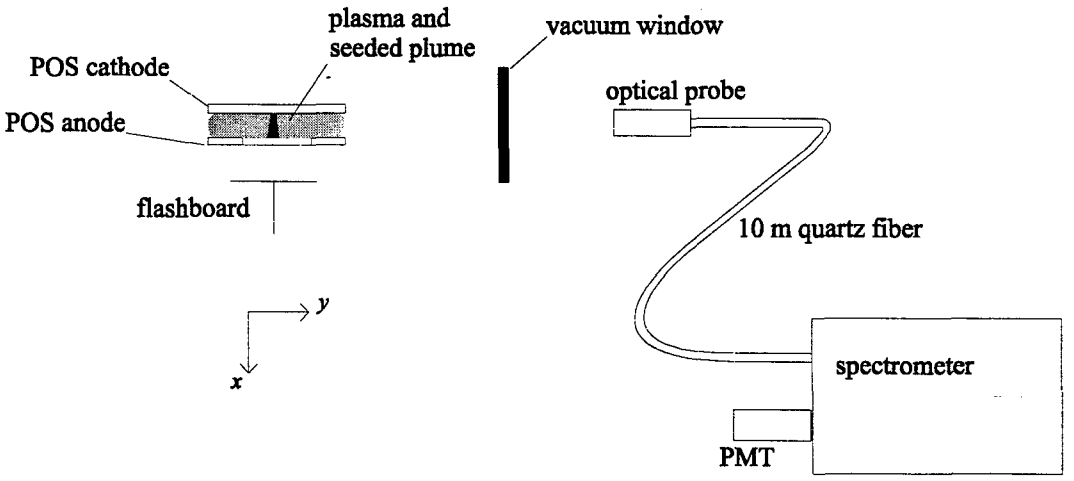

Figure 18. A schematic showing the apparatus for observing optical spectra from the POS gap using a spectrometer and PMT. In this illustration we show the probe viewing the plasma along the $y(\theta)$ direction. Axial views were also possible.

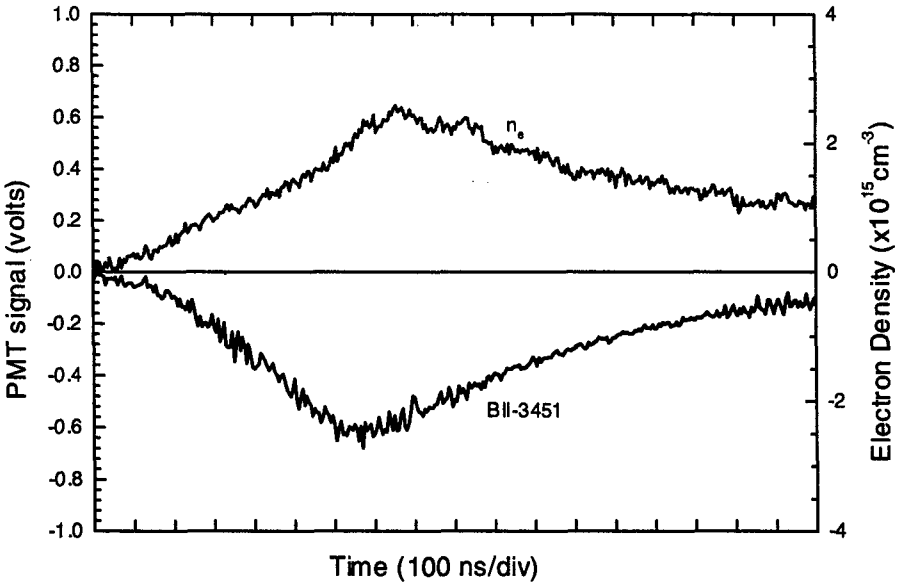

Figure 19. A plot showing the PMT signal centered on the B II-3451 Å line and the electron density (n_e) as a function of time. The electron density was determined from heterodyne interferometry along the same line-of-sight. These types of observations were used to determine the spatial extent of the ablated plume.

In this section we will show the measurements that were made to determine the spatial extent of the ablated plume for both ablation methods. This was accomplished by observing specific emission lines of the material as a function of the axial position in the planar switch. To excite and ionize the ablated material the flashboard plasma was also discharged a few microseconds after the laser was fired. Without such excitation emission from ablated material was never observed. The generator was not used for these measurements.

To observe this emission we used a photo-multiplier tube detector (PMT) in place of the ICCD camera and a single optical fiber as schematically shown in Figure 18. This detector was better suited for this type of measurement because the spectral characteristics of the line were unimportant. Once we verified that the that line was sufficiently isolated spectrally, we set up the PMT so it collected light from the entire line. Therefore a time history of that line was measured. Figure 19 shows an example of the time history of the B II-3451 Å line as a function of time along with the electron density due to the flashboard plasma.

In general, we would make two or three observations at each axial position and average the result. The spatial resolution for these measurements was 4 mm.

Figure 20(a) shows the relative intensity of the B II-3451 Å line and the Li I-6708 Å as a function of axial position in the switch. These observations were made with a single probe positioned to view the radial center and varied in the axial direction. For the boron observation we used a solid target of boron powder mixed with epoxy that was embedded in the anode. For the lithium observations we used a glass slide coated with LiF located outside the cathode. Each data point represents the peak light intensity as recorded by the PMT with the maximum normalized to unity. As Figure 20(a) shows the spatial distribution is roughly similar for both methods with a 2.5 cm fwhm.

Figure 20(b) shows the effect of a limiting aperture on the film ablation method with LiF. For this set of data the cathode aperture, through which the ablated plume passes, was limited to 0.56 mm. This resulted in a much narrower column as the data in Figure 20(b) reflect. In the radial center the width of the plume had been reduced to 0.7 cm. We also show the data taken near the anode and cathode that show reasonable collimation.

4.4 Characterization of the POS Plasma.

In this section we will report the measurements that were made on the intrinsic plasma, both with and without seeded material, to determine the electron temperature of the switch plasma during the conduction phase. Using time dependent collisional radiative

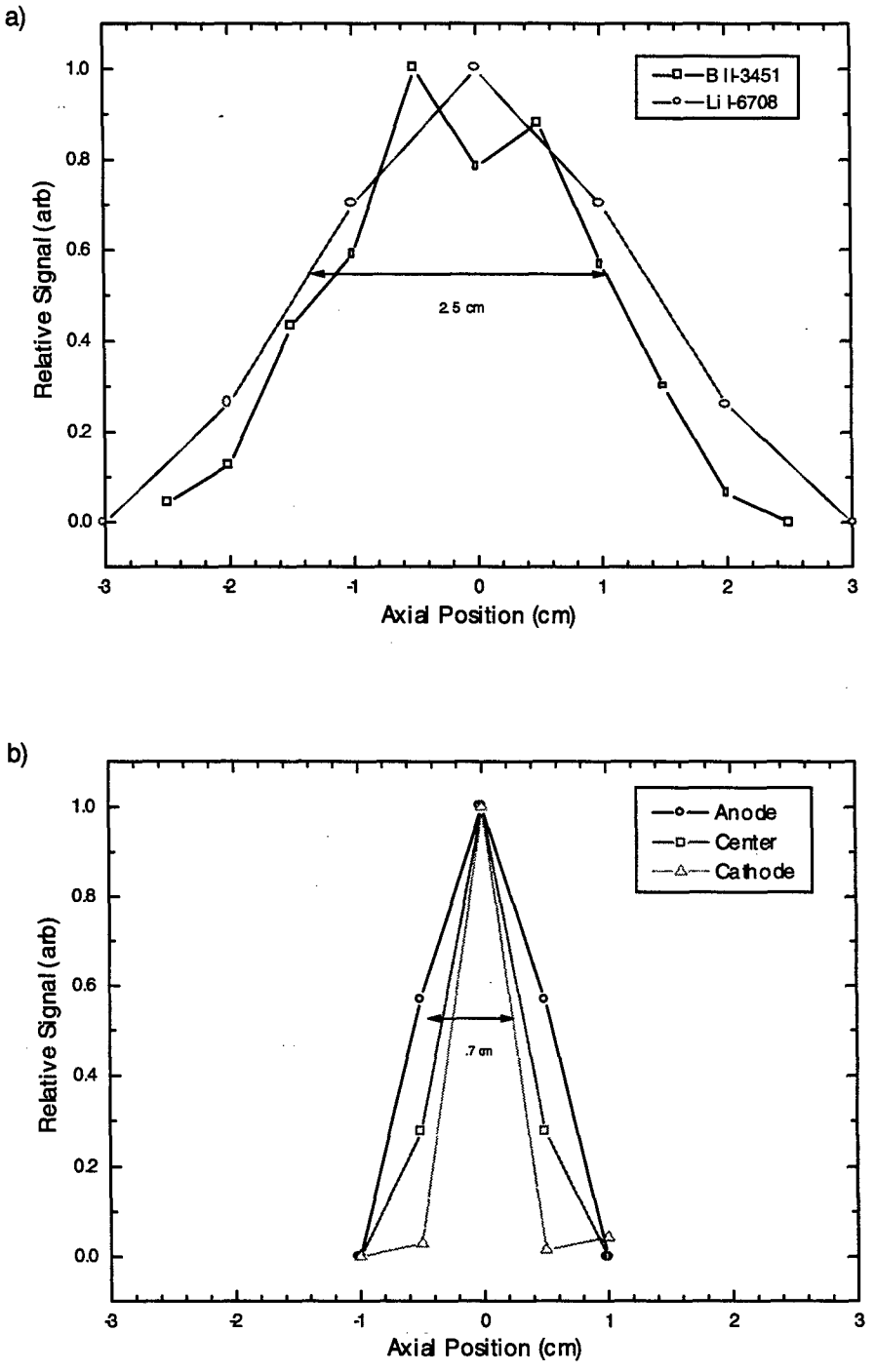

Figure 20. The axial distribution of the ablated plume where each plot has been normalized to unity. Part (a) shows the result in the radial center of the POS with no collimation for the solid boron target and LiF coated glass slide. Part (b) shows the results for the Li glass slide when the axial slot in the cathode was masked to 0.56 mm.

codes developed by Dr. Maron of Plasma Analyses, we were able to characterize this plasma. By modeling the plasma we determined the electron temperature (T_e) which is the key parameter (along with the electron density) is determining lifetimes of seeded ions. As inputs to the code we used the y averaged electron density as measured by heterodyne interferometry, and optical emission from carbon and magnesium in the plasma. The carbon used for these studies was not seeded material, rather a constituent of the flashboard plasma, whereas the Mg was seeded via ablation off glass slides. The most important lines that we observed were the C II 2836 Å and 4267 Å lines, which we used together to get the electron temperature. We also found the observations of Mg II were helpful in characterizing this plasma as well as illustrating the problems that one has with limited lifetimes of seeded ions.

To record these observations we used an apparatus consisting of a single optical probe/PMT detector shown in Figure 18. The relative isolation of the line was first checked with the ICCD camera attached to the spectrometer. Then a few shots had to be taken to make sure that the spectrometer was centered on the line. Once the system was set, full time histories of a single line were obtained on every shot with the proviso that no lines were nearby.

For the case of the C II emission at 2836 Å and the Mg II at 2800 Å, we used a different monochromator from that shown in Figure 2. A 0.33 m VUV Acton was used for these measurements. This is a small instrument that was easy to set up and has good transmittance in the UV region of the spectrum, it is not very good for resolving fine details, but is adequate for measuring an entire line. To conduct these measurements we carefully aligned the HeNe interferometer beam so it sampled the same volume of plasma as the optical probe. That way we could get the density information from the same region of the plasma. The spatial resolution of the interferometer is slightly larger (5 mm) than the optical probe. The time evolution of the C II (2836) and the Mg II (2800) lines are shown in Figure 21. Part (a) shows the results for carbon and (b) for magnesium. The results for Mg illustrate the problems that one has with lifetimes during the conduction phase. One would expect that during this phase of the POS the electron temperature would be increasing due to current flow. This can cause further ionization of ions such as Mg II and reduced its line radiation. In fact we see that the light emission decreases dramatically during the conduction phase.

Similar time histories were measured for C I, C III, and C IV. In addition, the ratio of the C II 4267 to 6578 lines was measured for the flashboard plasma (no generator) using the gated camera and the McPherson monochromator. This allowed us to determine that the initial electron temperature was in the 1.3-2 eV range. Using the time histories of various

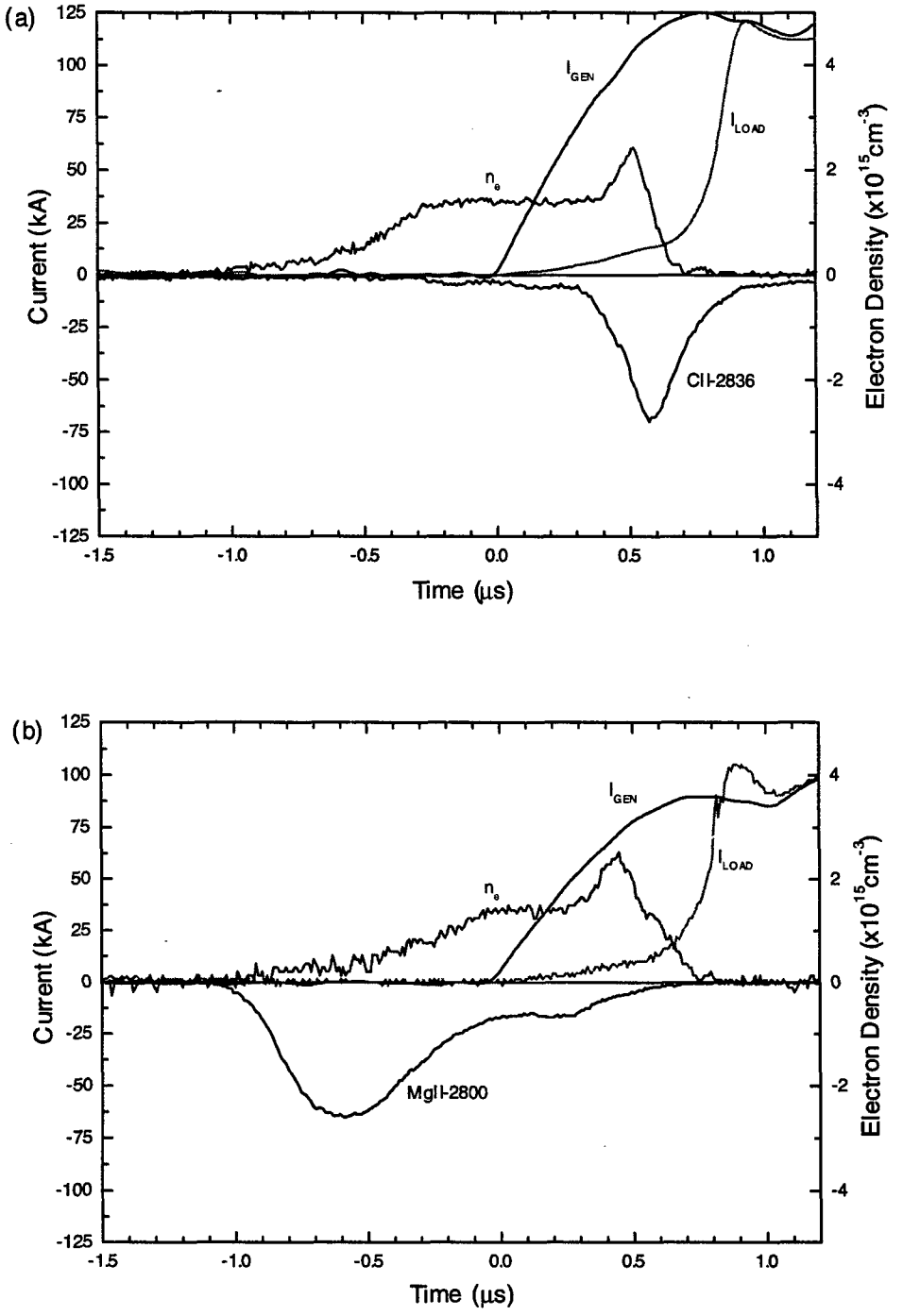

Figure 21. Examples of spectroscopic measurements showing the time histories of emission lines using a PMT detector during a shot. Part (a) shows the C II-2836 Å and part (b) the Mg II triplet at 2800 Å. The electron density was determined from heterodyne interferometry along the same line-of-sight as the optical probe. The load and generator currents for the shot are also shown.

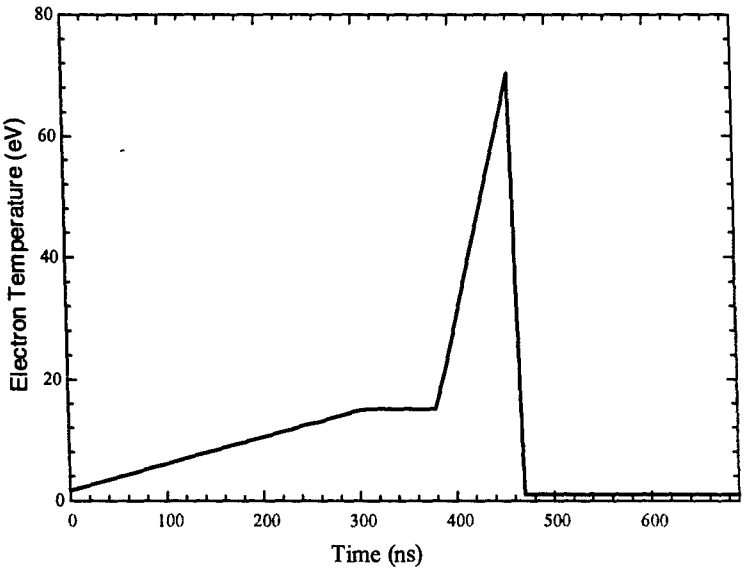

Figure 22. The predicted time evolution of the electron temperature for the POS at HY-Tech. An initial temperature of 2 eV was used and $t = 0$ corresponds to the beginning of the generator current.

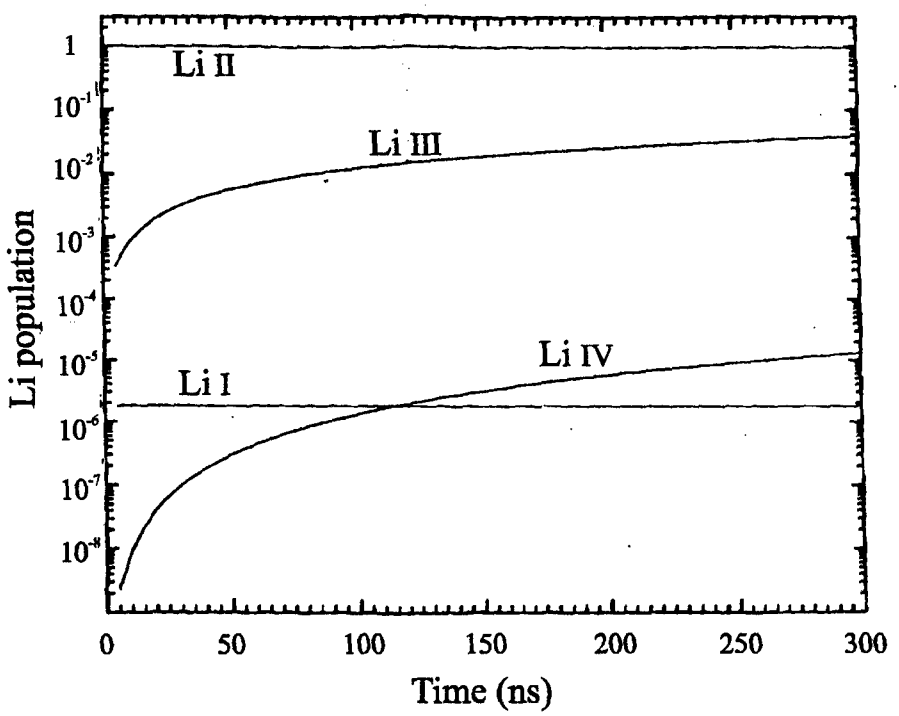

Figure 23. The predicted relative charge state populations as a function of time for conditions similar to the HY-Tech planar POS. A constant temperature of 20 eV and density of $1 \times 10^{15}\text{cm}^{-3}$ was used. This predicts that Li II essentially does not ionize.

lines, the electron density data, and the initial electron temperature, a predicted electron temperature evolution was determined by Plasma Analyses. This result is shown in Figure 22 where one can see that the electron temperature peaks at around 70 eV.
This is an important result because it gives confidence that certain ions will exist, such as Li II that has an ionization potential of 75 eV. Figure 23 shows a calculation performed by Plasma Analyses that predicts the relative Li charge state populations for average plasma conditions appropriate during the conduction phase of the POS ($< T_e >$=20 eV, $< n_e >= 10^{15}$ cm^{-3}). One can see that the Li^+ population changes very little in 300 ns with only 3% Li^{2+}. The implication is that if we observe Li^+ in the switch it will most likely exist for the entire conduction phase.
For other switches calculations like that shown in Figure 23 are essential to choose the specific ion that needs to be seeded and the charge state that is likely to persist. This will also have an impact on the method of calculation for the magnetic field that is best suited for a specific switch.

4.5 Implementation on Other Opening Switches.

Although resources did not permit us to complete a field measurement on the planar switch at HY-Tech, we have gained enough knowledge to recommend a procedure for any POS. This procedure must start with characterization measurements on the switch plasma during the conduction phase. The key to these characterization measurements is to get an estimate of the electron temperature so an educated guess, as to both the analysis method and the seed material, can be made. This is most easily accomplished by measuring the time histories (using PMTs) of select lines of the intrinsic plasma or seeded material. Figure 24 illustrates the importance of this characterization as we show data that was taken on the planar switch with two different seed materials. Part (a) shows the time history of the Li II 5484 Å line and part (b) the B II 3451 Å line. In the first case the lithium line is not observed until very late in the conduction phase when the switch first starts to open. The boron line is almost completely gone by the time the generator current starts. Based on these observations the lithium line might be suitable for either hotter, or longer conduction time switches where the ion acceleration method is used.
This characterization does not need to be detailed, but it must answer the fundamental question of which ion charge states will exist, and for how long, during the conduction phase. This should allow us to decide on which method is best suited for measuring the field. For Zeeman analysis ions with a low charge-to-mass ratio (q/m), or neutrals, would work the best because the Doppler broadening would be minimized. Single ionized barium

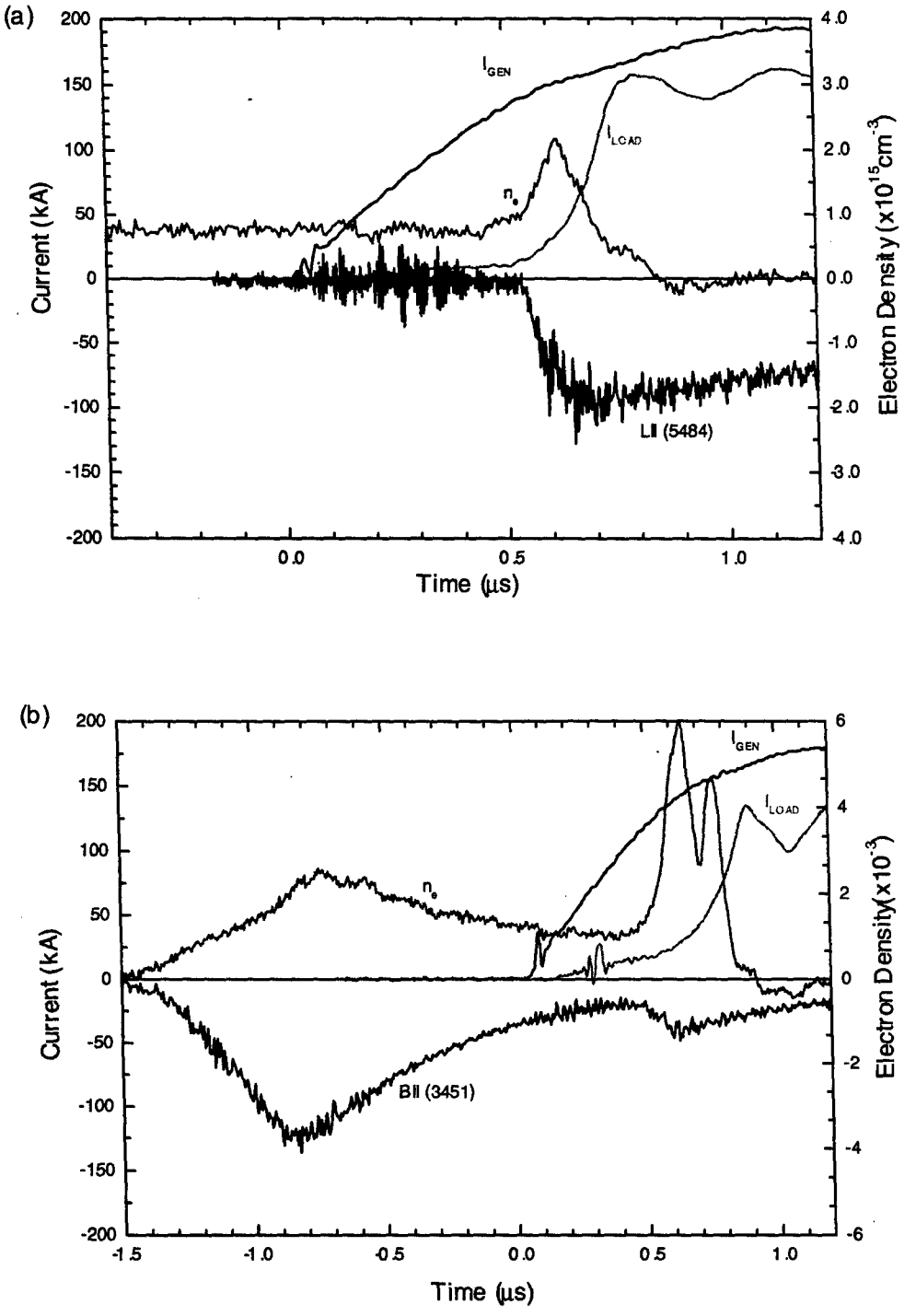

Figure 24. Measurements showing the time evolution of emission lines of seeded material during a shot. These measurements were made with a PMT attached to the McPherson spectrometer. Part (a) shows the Li II-5484 Å line that appears just before opening and part (b) the B II-3451 Åline.

(Ba II) is one such candidate for this type of analysis.[11] The ideal candidate for the ion velocity measurement is almost the exact opposite of the Zeeman analysis where light ions with large values of q/m are sought. These ions are more likely (compared to low q/m ions) to be accelerated to velocities that are measurable. Some possibilities in order of desirability are B III-2066 Å, Li II-5484 Å, B II-3451 Å, and Al III-4529 Å.

Because the Zeeman method is more direct, it is the preferred technique if suitable ions exist in the plasma. Based on our experiences with the planar switch at HY-Tech, and published experiments using shorter conduction time switches,[11] the Zeeman method has the best chance of success with shorter conduction time switches. For these switches the electron temperature is likely to be lower for a larger percentage of the conduction phase and Ba II may persist. A POS such as DM1 may be such a candidate.

For longer conduction time switches, such as ACE-4, the Zeeman method will most likely fail and we must rely on the acceleration of ions. As a result we must seek ions with large q/m ratios. For this type of switch Li II may be the ideal seed material due to the very large ionization potential of this ion (75 eV). It is quite probable that no switch will ionize Li II, and if it exists it will persist throughout the conduction phase. On the planar POS Li II was formed late in the conduction phase and could be used at that time. However, ACE-4 is a higher current density and longer conduction time so it is likely that Li II will exist for a substantial fraction of the conduction phase.

Section 5
Conclusions

We have fabricated and tested a two dimensional electron density diagnostic with high spatial resolution and throughput. Due to its excellent spatial resolution (100 μm) this instrument is particularly useful for viewing plasma formation near surfaces that may be due to adsorbed impurities. While its sensitivity to electron density is about a factor of 4 lower that heterodyne interferometry with a HeNe laser, the two methods are complementary, and both should be used in a switch. Heterodyne interferometry yields the time history of the electron density at one point in space and this interferometer gives the electron density over a two dimensional region at one point in time.

For the diagnostic to determine the two dimensional current density we were not able to make a field measurement. However, we did obtain a significant amount of knowledge with regard to seeding techniques to be used in concert with emission spectroscopy. In fact, an additional seeding technique employing a small gas puff has been successfully used,[13] and should be considered as an option for future work. These are very powerful diagnostic tools that need some more refinement to produce a working instrument. While a similar technique has been used in the past to measure the current distribution on a short conduction time switch,[12, 10, 11] the situation is more complicated for longer conduction time switches with higher IT products. The development of these techniques, and the knowledge gained during this program, has enabled us to predict seed materials and analysis techniques that have a good chance of working on ACE-4 and DM1.

Appendix
Bibliography

G.G. Spanjers, E.J. Yadlowsky, R.C. Hazelton, and J.J. Moschella, "Ion Mass Effects in Plasma Opening Switches,"(UNCLASSIFIED) DNA Technical Report, Contract DNA001-92-C-0034, (1995).(UNCLASSIFIED)

W. Rix, A.R. Miller, J. Thompson, E. Waisman, M. Wilinson, A. Wilson, "Pulsed Power Inductive Energy Storage in the Microsecond Range,"(UNCLASSIFIED) in *Proceedings of the 9th International Conference on High-Power Particle Beams*, D. Mosher and G. Cooperstein eds., Washington D.C. (1993) p. 402.(UNCLASSIFIED)

W.W. Macy, Jr., "Two-Dimensional Fringe-Pattern Analysis,"(UNCLASSIFIED) Appl. Opt. **22**(23), 3898 (1983).(UNCLASSIFIED)

B.V. Weber and D.D. Hinshelwood, "He-Ne Interferometer for Density Measurements in Plasma Opening Switch Experiments,"(UNCLASSIFIED) Rev. Sci. Instrum. **63**(10), 5199 (1992).(UNCLASSIFIED)

G.G. Spanjers, E.J. Yadlowsky, R.C. Hazelton, and J.J. Moschella, "Characterization of magnetohydrodynamic effects in a plasma opening switch,"(UNCLASSIFIED) J. Appl. Phys. **77**(8), 3657 (1995).(UNCLASSIFIED)

N.R. Pereira, J.R. Goyer, D. Kortbawi, J.R. Thompson, and S.E. Davis, "Operation of a heated POS in DM1," (UNCLASSIFIED) in *Proceedings of the 1999 IEEE International Conference on Plasma Science-Abstracts*, p. 277.(UNCLASSIFIED)

B.V. Weber, R.J. Commisso, R.A. Meger, J.M. Neri, W.F. Oliphant, and P.F. Ottinger, "Current Distribution in a Plasma Erosion Opening Switch,"(UNCLASSIFIED) Appl. Phys. Lett. **45**(10), 1043 (1984).(UNCLASSIFIED)

G.G. Spanjers, E.J. Yadlowsky, R.C. Hazelton, and J.J. Moschella, "Investigation of current channel migration in a conducting plasma between planar electrodes,"(UNCLASSIFIED) J. Appl. Phys. **79**(5), 2229 (1996).(UNCLASSIFIED)

J.E. Bailey, A.L. Carlson, R.L. Morrison, and Y. Maron, "Visible spectroscopy measurements in the PBFA II ion diode,"(UNCLASSIFIED) Rev. Sci. Instrum. **61**(10), 3075 (1990).(UNCLASSIFIED)

A. Weingarten, C. Grabowski, A. Fruchtman, and Y. Maron, "The time-dependent electron density and magnetic field distributions in a 70 ns plasma opening switch,"(UNCLASSIFIED) in *Proceedings of the 12th International Conference on High-Power Particle Beams*, Haifa, Israel.(to be published)

R. Shpitalnik, A. Weingarten, K. Gomberoff, Ya.E. Krasik, and Y. Maron, "Observations of two-dimensional magnetic field evolution in a plasma opening switch,"(UNCLASSIFIED) Phys. Plasmas **5**(3), 792 (1997).(UNCLASSIFIED)

M. Sarfaty, R. Shpitalnik, R. Arad, A. Weingarten, Ya.E. Krasik, A. Fructman, and Y. Maron, "Spectroscopic investigation of fast (ns) magnetic field penetration in a plasma,"(UNCLASSIFIED) Phys. Plasmas **2**(6), 2583 (1995).(UNCLASSIFIED)

R. Arad, L. Ding, and Y. Maron, "Novel gas-doping technique for local spectroscopic measurements in pulsed-power systems,"(UNCLASSIFIED) Rev. Sci. Instrum. **69**(3), 1529 (1998).(UNCLASSIFIED)

I.H. Hutchinson, *Principles of Plasma Diagnostics*(UNCLASSIFIED), (Cambridge Univ. Press, Cambridge MA, 1987) Chapter 4.(UNCLASSIFIED)

M. Takeda, H. Ina, and S. Kobayashi, "Fourier-Transform Method of Fringe-Pattern Analysis for Computer-Based Topography and Interferometry,"(UNCLASSIFIED) J. Opt. Soc. Am. **72**(1), 156 (1982).(UNCLASSIFIED)

D.J. Bone, H.A. Bachor, and R.J. Sandemen, "Fringe-pattern analysis using a 2-D Fourier transform,"(UNCLASSIFIED) Appl. Optics **25**(10), 1653 (1986).(UNCLASSIFIED)

DEPARTMENT OF DEFENSE

DEFENSE TECHNICAL
INFORMATION CENTER
8725 JOHN J. KINGMAN ROAD,
SUITE 0944
FT. BELVOIR, VA 22060-6201
2 CYS ATTN: DTIC/OCA

DEFENSE THREAT REDUCTION
AGENCY
8725 JOHN J. KINGMAN ROAD,
STOP 6201
FT. BELVOIR, VA 22060-6201
2 CYS ATTN: NT/R. DAVIS

DEPARTMENT OF DEFENSE CONTRACTORS

ITT INDUSTRIES
ITT SYSTEMS CORPORATION
1680 TEXAS STREET, SE
KIRTLAND AFB, NM 87117-5669
2 CYS ATTN: DTRIAC
ATTN: DARE

HY-TECH RESEARCH
CORPORATION
104 CENTRE COURT
RADFORD, VA 24141
ATTN: J. MOSCHELLA